JOURNAL OF **UMALCA**
Unión Matemática
de América Latina y el Caribe

ORBITA MATHEMATICAE

Estimation of persistence diagrams via the three-gap theorem

Luis Suarez Salas and Jose A. Perea

msp

vol. 3 no. 1 2026

ORBITA
MATHEMATICAE

Vol. 3, No. 1, 2026
https://doi.org/10.2140/om.2026.3.1

msp

Estimation of persistence diagrams via the three-gap theorem

Luis Suarez Salas and Jose A. Perea

The time delay (or sliding-window) embedding is a technique from dynamical systems to reconstruct attractors from time-series data. Recently, descriptors from topological data analysis (TDA) — specifically, persistence diagrams — have been used to measure the shape of said reconstructed attractors in applications including periodicity and quasiperiodicity quantification. Despite their utility, the fast computation of persistence diagrams of sliding-window embeddings is still poorly understood. We present theoretical and computational schemes to approximate the persistence diagrams of sliding-window embeddings from quasiperiodic functions. We do so by combining the three-gap theorem from number theory with the persistent Künneth formula from TDA, and derive fast and provably correct persistent homology approximations. The input to our procedure is the spectrum of the signal, and we provide numerical as well as theoretical evidence of its utility to capture the shape of toroidal attractors.

1. Introduction

The sliding-window embedding is a powerful technique for reconstructing attractors of a dynamical system from observed time-series data. When combined with tools from topological data analysis (TDA), such as persistence diagrams, one can measure the topological properties of the state space to detect patterns in the original signal. In general, combining sliding windows with persistence can be used to probe for the presence of nontrivial recurrent behavior. For example, Figure 1 depicts a system with behavior more complex than periodicity.

Indeed, leveraging measurements of the system, such as the horizontal position $x(t)$ of the block or the angular position $\theta(t)$ of the pendulum, one can determine (as we will explain below) that the system exhibits a type of recurrent behavior known as *quasiperiodicity* (Figure 3 and Section 2.2). In dynamical systems this behavior emerges when oscillators are superimposed, also in the transition between stable and chaotic dynamics [Weixing et al. 1993], and has been observed, for instance, in fMRI scans obtained from mice [Belloy et al. 2017], in the formation of quasicrystals [Levine and Steinhardt 1984] and in the study of biphonation in mammal vocalization [Wilden et al. 1998].

Mathematically, we say that $f : \mathbb{R} \to \mathbb{C}$ is quasiperiodic (see Definition 2.29) with frequency vector $\omega = (\omega_1, \ldots, \omega_N)$ if $\{\omega_i\}_{i=1}^N$ are positive real numbers which are linearly independent over $\mathbb{Q}$ (i.e., incommensurate) and

$$f(t) = F(\omega_1 t, \ldots, \omega_N t),$$

This work was partially supported by the National Science Foundation through CAREER award DMS-2415445.
MSC2020: 37B20, 37E30, 55-08, 55N31, 55U25.
Keywords: persistence diagrams, persistent homology, topological data analysis, sliding-window embedding, quasiperiodic signals, three-gap theorem, continued fractions, Rips filtration, Künneth formula, time series analysis.

© 2026 The Authors, under license to MSP (Mathematical Sciences Publishers).

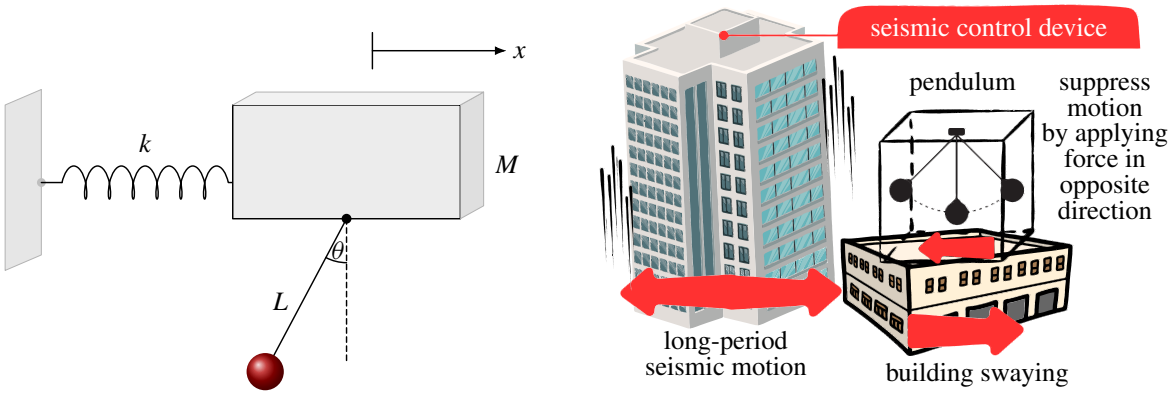

Figure 1. Left: schematic model for a pendulum on a sliding block. Right: illustration of antiearthquake technology (see also [Yirka 2013]), whose dynamics are captured by the model on the left.

where $F : \mathbb{T}^N \to \mathbb{C}$ is a complex-valued continuous function on the N-torus $\mathbb{T}^N = \mathbb{R}^N/\mathbb{Z}^N$, called the parent function of f [Gakhar and Perea 2024]. Note that in the case of a single frequency, f is just a periodic function.

Periodicity or quasiperiodicity in a signal with frequency vector of length N corresponds to observing the traversal of a (topological) circle or an N-torus attractor, respectively, in the phase space of the underlying dynamics [Skraba et al. 2012]. Takens' embedding theorem [1981], on the other hand, under appropriate conditions [Xu et al. 2019], ensures that the sliding-window embedding of the signal (Section 2.2 and Figure 2, center) provides a topological reconstruction of said attractors. Finally, periodicity/quasiperiodicity can be quantified with shape descriptors from TDA: the Rips persistence diagrams (defined in Section 2.1 and shown in Figure 2, right) of the reconstructed attractors via sliding-window embeddings. In short, they measure the prominence and dimension of holes in a point cloud, providing a convenient summary of its multiscale geometry and topology.

Much work has been done to establish the usefulness of sliding windows and persistence, with applications including parameter estimation in damping mechanisms [Myers and Khasawneh 2022], stability of stochastic delay equations [Khasawneh and Munch 2016], quantifying the presence of biphonation in vibrating vocal folds [Tralie and Perea 2018] and periodicity detection in gene expression data [Perea et al. 2015]. Furthermore, there are well-defined methodologies for optimizing the embedding parameters of the sliding-window embedding, in such a way that the topological features in the persistence diagrams are maximally amplified [Gakhar and Perea 2024]. However, the algorithmic complexity of computing the persistent homology of Rips filtrations remains a challenge in real-world applications. This is the case even with highly optimized libraries like Ripser [Bauer 2021], which exploits cohomology duality, apparent pairs and clearing optimizations to achieve substantial speed-ups. The main difficulty lies in that the worst-case complexity of the matrix-reduction algorithm [Zomorodian and Carlsson 2005] for computing persistent homology in degrees $j = 0, \ldots, J$ is cubic in the number of simplices of dimensions $0, \ldots, J+1$ [Morozov 2005]; the case relevant to us is $J = N$, i.e., the number of $\mathbb{Q}$-linearly

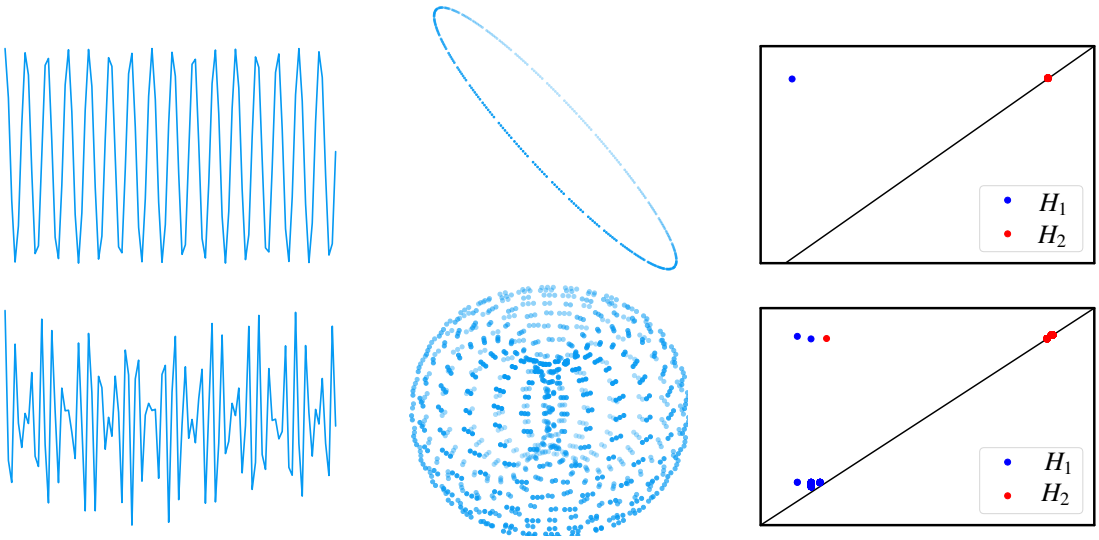

Figure 2. Given a time series (left column), we reconstruct the underlying attractor via its sliding-window embedding (middle column), and then compute its persistent homology (right column). Top row: the signal from the periodic motion of an ideal pendulum (left). The sliding-window point cloud parametrizes a circle (middle), so its persistence diagram exhibits exactly one nontrivial 1-dimensional homology class (right). Bottom row: A quasiperiodic function with two incommensurate frequencies (left); its sliding-window embedding (center) recovers a 2-torus. The corresponding persistence diagrams (right) confirm this topology by showing two independent 1-dimensional classes and one 2-dimensional class.

independent frequencies in the signal f. Moreover, the number of j-dimensional simplices for Ripser grows as $\binom{n_{\mathrm{SW}}}{j+1}$, where n_{SW} is the number of points in the sliding-window embedding. In practice, this proves to be computationally taxing even when $N = 2$ and $n_{\mathrm{SW}} = 1000$, and motivates our efforts to develop approximation methods with known error bounds (see Figure 3) that would provide a faster and computationally accessible alternative (see Figure 11 and Table 2). Our method relies on the three-gap theorem, which uses continued-fraction expansions from number theory to describe how points — sampled at irrational rotation angles — are distributed around a circle. We also use the Künneth formula in persistent homology. Thanks to the results in Section 2.3, our pipeline applies to a general quasiperiodic function f. It suffices to compute the spectrum of f — e.g., via the fast Fourier transform (FFT) — to obtain the input to our algorithm (Section 2.5). Specifically, we replace the standard Ripser-based step 3 by our two-part alternative (3b) shown below (we keep the original procedure as step (3a) for comparison).

(1) Start with a time series f.

(2) Reconstruct the phase space by computing $\{\mathrm{SW}_{d,\tau} f(t)\}_{t=0}^{T}$.

(3a) Compute $\mathrm{dgm}_j^R(\{\mathrm{SW}_{d,\tau} f(t)\}_{t=0}^{T}, d_2)$ using Ripser.

(3b) (i) Use the FFT to retrieve the frequencies of f and then compute their continued-fraction expansion (CFE).

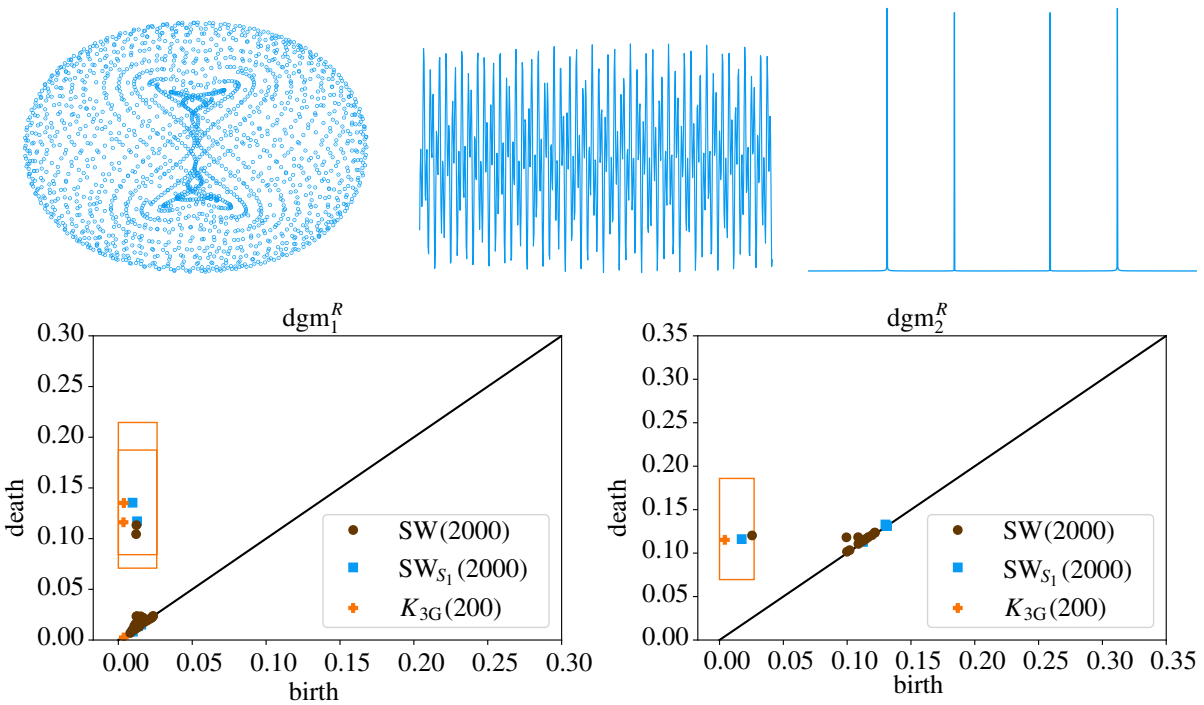

Figure 3. Top row: the plot on the left is the phase space $(x, \dot{x})$ from the pendulum attached to a sliding block shown in Figure 1. The solution $x(t)$ we used for the sliding-window embedding is plotted in the middle, followed by the modulus of its discrete Fourier transform on the right. Bottom row: persistence diagrams of the sliding-window embedding of $x(t)$ (brown circles) of a truncated Fourier series of $x(t)$ (blue squares), and our proposed approximation K_{3G} (orange crosses). The orange rectangles depict the theoretical approximation bound.

(ii) Use the CFE as shown in Section 3 and then apply the results from Section 4 to approximate $\mathrm{dgm}_j^R(\{\mathrm{SW}_{d,\tau} f(t)\}_{t=0}^T, d_2)$ for $j = 1, 2$.

In step (3b)(ii), the continued-fraction expansions allow us to compute exact persistence diagrams on each frequency circle (via the three-gap theorem; see Section 3), which we then assemble — using the Künneth formula as detailed in Section 4 — to approximate the persistence diagrams of interest.

Remark 1. The idea of using Fourier analysis together with the Künneth formula to compute persistent homology is not unique to our work. Indeed, in [Kim and Jung 2026], these tools are combined to construct a multiparameter filtration whose persistent homology can be computed exactly. As the authors state:

> Our main idea is to transform time-series data into a barcode through the Liouville torus without utilizing sliding-window embedding.

Thus their method depends on reconstructing the full Liouville torus.

feature	our 3G method	method of [Kim and Jung 2026]
FFT-based decomposition	yes	yes
Künneth-type product formula	yes	yes
Takens' theorem	yes	yes
sliding-window embedding	yes	no
Liouville torus	no	yes
continued fraction expansion	yes	no
filtration type	1-parameter	multiparameter
type of signal	quasiperiodic	periodic
exactness vs. approximation	approximate (error bound)	exact

Table 1. At-a-glance comparison of our 3G pipeline vs. the exact multiparameter method of [Kim and Jung 2026].

By contrast, our work approximates the persistence diagram via a single-parameter sliding-window Rips filtration

$$f \longrightarrow R_\epsilon(\mathrm{SW}_{d,\tau} f) \longrightarrow \mathrm{dgm}_j^R(\mathrm{SW}_{d,\tau} f).$$

(time-series data) (Rips complex of sliding-window embedding) (persistence diagram)

Meanwhile, [Kim and Jung 2026] provides exact formulas for the persistence diagram of the Liouville torus Ψ_f, obtained from the multiparameter filtration

$$f \longrightarrow R_{\epsilon_1}(\pi_1\Psi_f) \times \cdots \times R_{\epsilon_N}(\pi_N\Psi_f) \longrightarrow \mathrm{dgm}_j^{R,l}(\Psi_f).$$

(time-series data) (multiparameter filtration of the Liouville torus) (persistence diagram)

We summarize the distinguishing features of these two methods in Table 1.

2. Background and definitions

In this section we cover the mathematical concepts needed for our three-gap (3G) method. We first define persistence modules, their barcodes and stability theory, and the special case of persistent homology for filtered simplicial complexes. Next we introduce dynamical systems and highlight Takens' reconstruction theorem, which underlies the sliding-window embedding. After that, we show how the Fourier transform recovers the frequency vector of a general quasiperiodic signal. We then recall continued-fraction expansions and their fundamental properties, leading directly to the three-gap theorem — the number-theoretic pillar of our work. We conclude with an overview of our 3G method (named for its use of the three-gap theorem), emphasizing how these components fit together.

2.1. ***Persistent homology.*** Our presentation of persistence modules and their interleaving distance follows [Chazal et al. 2016, Chapters 1, 3 and 4]. These concepts provide an algebraic account of stability, used herein.

2.1.1. *Persistence modules.*

Definition 2.1. A persistence module $\mathbb{V}$ over the real numbers $\mathbb{R}$ is an indexed family of vector spaces

$$\{V_t \mid t \in \mathbb{R}\},$$

together with a doubly indexed family of linear maps

$$\{v_s^t : V_s \to V_t \mid s \leq t\}$$

which satisfy the composition law

$$v_s^t \circ v_r^s = v_r^t$$

whenever $r \leq s \leq t$, and where v_t^t is the identity map on V_t for every $t \in \mathbb{R}$.

Definition 2.2. A morphism Φ between two persistence modules $\mathbb{U}$ and $\mathbb{V}$ is a collection of linear maps

$$\varphi_t : U_t \to V_t$$

such that the diagram

$$\begin{array}{ccc} U_s & \xrightarrow{u_s^t} & U_t \\ {\scriptstyle \varphi_s}\downarrow & & \downarrow{\scriptstyle \varphi_t} \\ V_s & \xrightarrow{v_s^t} & V_t \end{array}$$

commutes for all $s \leq t$. Composition is defined in the obvious way, as are identity morphisms. This makes the collection of persistence modules into a category. The set of all morphisms from $\mathbb{U}$ to $\mathbb{V}$ is denoted by

$$\mathrm{Hom}(\mathbb{U}, \mathbb{V}).$$

When $\mathbb{U} = \mathbb{V}$, these are called *endomorphisms*, and we write

$$\mathrm{End}(\mathbb{V}) = \mathrm{Hom}(\mathbb{V}, \mathbb{V}).$$

We have the following generalization of a morphism:

Definition 2.3. Let $\mathbb{U} = \{U_t, u_s^t\}$ and $\mathbb{V} = \{V_t, v_s^t\}$ be persistence modules indexed by $t \in \mathbb{R}$. A *morphism of degree* $\delta \geq 0$ is a family of linear maps

$$\varphi_t : U_t \to V_{t+\delta} \quad \text{for } t \in \mathbb{R},$$

such that for all $s \leq t$ the square

$$\begin{array}{ccc} U_s & \xrightarrow{u_s^t} & U_t \\ {\scriptstyle \varphi_s}\downarrow & & \downarrow{\scriptstyle \varphi_t} \\ V_{s+\delta} & \xrightarrow{v_{s+\delta}^{t+\delta}} & V_{t+\delta} \end{array}$$

commutes. We write

$$\mathrm{Hom}^{\delta}(\mathbb{U}, \mathbb{V}) = \{\varphi \text{ of degree } \delta\}.$$

When $\mathbb{U} = \mathbb{V}$, such a map is called a *degree-δ endomorphism*, and we write

$$\mathrm{End}^\delta(\mathbb{V}) = \mathrm{Hom}^\delta(\mathbb{V}, \mathbb{V}).$$

Definition 2.4. For any persistence module $\mathbb{V} = \{V_t, v_s^t\}$ and $\delta \geq 0$, the *shift map*

$$1_{\mathbb{V}}^\delta = \{v_t^{t+\delta} \mid V_t \to V_{t+\delta}\}_{t\in\mathbb{R}}$$

is a degree-δ endomorphism in $\mathrm{End}^\delta(\mathbb{V})$.

Definition 2.5. Let $\mathbb{U}$ and $\mathbb{V}$ be persistence modules and fix $\delta \geq 0$. A *δ-interleaving* consists of

$$\Phi \in \mathrm{Hom}^\delta(\mathbb{U}, \mathbb{V}) \quad \text{and} \quad \Psi \in \mathrm{Hom}^\delta(\mathbb{V}, \mathbb{U}),$$

such that

$$\Psi\Phi = 1_{\mathbb{U}}^{2\delta} \quad \text{and} \quad \Phi\Psi = 1_{\mathbb{V}}^{2\delta}.$$

Definition 2.6. The *interleaving distance* between two persistence modules $\mathbb{U}$ and $\mathbb{V}$ is

$$d_I(\mathbb{U}, \mathbb{V}) = \inf\{\delta \geq 0 \mid \mathbb{U} \text{ and } \mathbb{V} \text{ admit a } \delta\text{-interleaving}\}.$$

If no finite δ exists, set $d_I(\mathbb{U}, \mathbb{V}) = \infty$.

Under appropriate finiteness conditions, which we describe below, a persistence module can be uniquely determined up to isomorphism by an invariant called the *barcode*. Indeed, first note that the direct sum of persistence modules can be defined componentwise; that is, $\mathbb{U} \oplus \mathbb{V}$ has vector spaces $U_t \oplus V_t$ (direct sum of vector spaces) and linear maps $v_s^t \oplus u_s^t$.

Definition 2.7. Let $\mathbb{V}$ be a persistence module such that V_t is finite dimensional for each $t \in \mathbb{R}$ (i.e., $\mathbb{V}$ is pointwise finite). By [Crawley-Boevey 2015], there is a unique multiset $\mathrm{bcd}(\mathbb{V})$ of intervals $I \subseteq \mathbb{R}$, called the barcode of $\mathbb{V}$, such that

$$\mathbb{V} \cong \bigoplus_{I\in\mathrm{bcd}(\mathbb{V})} \mathbb{I}_I,$$

where $\mathbb{I}_I$ is the persistence module with vector spaces the field $\mathbb{F}$ for each $t \in I$ and the zero vector space otherwise, and linear maps the identity whenever possible and the zero map when not. By multiset we mean that intervals may appear with finite repetition (multiplicity). The persistence diagram of $\mathbb{V}$ is the following multiset of points in the extended plane $\overline{\mathbb{R}}^2 = [-\infty, \infty] \times [-\infty, \infty]$:

$$\mathrm{dgm}(\mathbb{V}) = \{(\inf(I), \sup(I)) \mid I \in \mathrm{bcd}(\mathbb{V})\}.$$

The space of persistence diagrams can be endowed with an extended pseudometric called the bottleneck distance d_B [Cohen-Steiner et al. 2007; Chazal et al. 2016]. In the following definition we consider the points in the diagonal $y = x$ as part of the persistence diagrams; moreover, each point (x, x) is included with countable infinite multiplicity.

Definition 2.8. Let $\mathrm{dgm}, \mathrm{dgm}' \subseteq \overline{\mathbb{R}}^2$ be two persistence diagrams. Their bottleneck distance is

$$d_B(\mathrm{dgm}, \mathrm{dgm}') = \inf_{\phi:\mathrm{dgm}\to\mathrm{dgm}'} \sup_{y\in\mathrm{dgm}} \{\|y - \phi(y)\|_\infty\},$$

where ϕ is a bijection of multisets and $\|(a, b)\|_\infty = \max\{|a|, |b|\}$ is the extended sup norm on $\overline{\mathbb{R}}^2$.

Conceptually, given two persistence diagrams we consider all multiset bijections that pair points between them. The distortion of a given pairing can be quantified using the largest infinity norm over all paired points. The bottleneck distance is then the smallest possible distortion over all bijective pairings. In essence, this captures how similar two persistence diagrams are to each other in the plane. We note that including all points (x, x) along the diagonal ensures that any two diagrams admit a bijective matching (so that unmatched off-diagonal points may be paired with diagonal points).

The interleaving distance between persistence modules and the bottleneck distance between their persistence diagrams satisfy the celebrated isometry theorem [Lesnick 2015],

Theorem 2.9. *Let $\mathbb{U}$ and $\mathbb{V}$ be pointwise finite persistence modules. Then*

$$d_I(\mathbb{U}, \mathbb{V}) = d_B(\mathrm{dgm}(\mathbb{U}), \mathrm{dgm}(\mathbb{V})).$$

2.1.2. *Persistent homology of filtered simplicial complexes.* In this section we describe a formal notion of "shape" for discrete data sets. Unless otherwise noted, definitions follow [Hatcher 2002; Gakhar and Perea 2024].

Definition 2.10. Given a set X, an abstract simplicial complex (or a simplicial complex, for short) with vertices in X is a subset $K \subseteq \mathcal{P}(X)$ of the power set of X, such that

(1) every $\sigma \in K$ is finite and nonempty,

(2) for any $\sigma \in K$, if $\tau \neq \varnothing$ and $\tau \subseteq \sigma$, then $\tau \in K$.

The elements of K are called simplices and the dimension of a simplex is one less than its cardinality: $\dim(\sigma) = |\sigma| - 1$. We also define $\dim(K) = \max\{\dim(\sigma) \mid \sigma \in K\}$. A face of σ is any nonempty proper subset of it. The n-th skeleton of K is denoted by $K^{(n)} := \{\sigma \in K \mid \dim(\sigma) \leq n\}$ for $n \in \mathbb{N} = \{0, 1, \ldots\}$; in particular, $K^{(0)}$ is called the set of vertices of K and $K^{(1)} \setminus K^{(0)}$ is its set of edges. A subcomplex of K is a subset $L \subseteq K$ which is also an abstract simplicial complex.

We can construct an abstract simplicial complex from any set of points in a metric space. Indeed, this is achieved via the *Rips complex*, which treats each point in a metric space (X, d), say $x \in X$, as a vertex; edges $\{x_0, x_1\}$ are created between two vertices if their distance is at most some fixed $\epsilon \geq 0$, i.e., $d(x_0, x_1) \leq \epsilon$; connecting three vertices creates a triangle $\{x_0, x_1, x_2\}$, four a tetrahedron $\{x_0, x_1, x_2, x_3\}$, and so on. Formally:

Definition 2.11. Given a metric space (X, d) and a real number ϵ, the Rips complex $R_\epsilon(X, d)$ is the simplicial complex

$$R_\epsilon(X, d) = \{\{x_0, \ldots, x_n\} \subseteq X \mid d(x_i, x_j) \leq \epsilon,\ \forall 0 \leq i, j \leq n\}.$$

With this construction we can leverage a powerful shape descriptor from algebraic topology — simplicial homology — which assigns algebraic objects to an abstract simplicial complex in a deformation-invariant manner. In particular, the 0-th dimensional homology measures the number of connected components, the 1-st dimensional homology detects loops, and the 2-nd dimensional homology detects cavities. In general, the n-th dimensional homology detects n-dimensional holes. The relevant definitions are below.

Definition 2.12. Let K be a simplicial complex and $\mathbb{F}$ a field. For $n \in \mathbb{N}$, let $C_n(K;\mathbb{F})$ denote the $\mathbb{F}$-vector space with basis the set of n-simplices of K:

$$C_n(K;\mathbb{F}) = \left\{ \sum_{\sigma \in K^{(n)} \smallsetminus K^{(n-1)}} a_\sigma \sigma \;\middle|\; a_\sigma \in \mathbb{F},\ a_\sigma \neq 0 \text{ for only finitely many } \sigma \right\}.$$

For $n < 0$, we let $C_n(K;\mathbb{F})$ be the zero vector space.

We call an element $\tau \in C_n(K;\mathbb{F})$ an *n-chain*. If

$$\tau = \sum_{\sigma \in K^{(n)} \smallsetminus K^{(n-1)}} a_\sigma \sigma$$

and σ_0 is one of the simplices in the sum (i.e., $a_{\sigma_0} \neq 0$), we write $\sigma_0 \in \tau$.

Definition 2.13. Fix a partial (e.g., a total) order $\preceq$ on the vertices of K so that each simplex $\sigma \in K$ is totally ordered. The n-th boundary map $\partial_n : C_n(K;\mathbb{F}) \to C_{n-1}(K;\mathbb{F})$ is the linear transformation defined for any $\sigma = \{v_0, \ldots, v_n\} \in K^{(n)} \smallsetminus K^{(n-1)}$ as

$$\partial_n(\sigma) = \sum_{i=0}^{n} (-1)^n \{v_0, \ldots, \hat{v_i}, \ldots, v_n\},$$

where $v_i \preceq v_{i+1}$ for $i = 0, \ldots, n-1$, and $\{v_0, \ldots, \hat{v_i}, \ldots, v_n\}$ denotes the $(n-1)$-th face of σ obtained by removing the i-th vertex v_i from the totally ordered set $\{v_0, \ldots, v_n\}$.

One can show that $\partial_n \circ \partial_{n+1} = 0$ for all $n \in \mathbb{N}$.

Definition 2.14. For $n \in \mathbb{N}$, a field $\mathbb{F}$ and a simplicial complex K, let

$$\ker(\partial_n) = \{\tau \in C_n(K;\mathbb{F}) \mid \partial_n(\tau) = 0\} \quad \text{and} \quad \operatorname{im}(\partial_{n+1}) = \{\partial_{n+1}(\beta) \mid \beta \in C_{n+1}(K;\mathbb{F})\} \subseteq \ker(\partial_n).$$

The n-th homology of K with coefficients in $\mathbb{F}$ is the quotient vector space

$$H_n(K;\mathbb{F}) = \frac{\ker(\partial_n)}{\operatorname{im}(\partial_{n+1})}.$$

We note that the isomorphism type of $H_n(K;\mathbb{F})$ is independent of the partial order on the vertices of K. Moreover, when $K = R_\epsilon(X,d)$ and $\epsilon \geq 0$, the nonzero elements of $H_n(R_\epsilon(X,d);\mathbb{F})$ correspond to nontrivial n-cycles (i.e., elements of $\ker(\partial_n)$) not bounding any $(n+1)$-chain in the Rips complex $R_\epsilon(X,d)$, and thus measure n-dimensional holes in (X,d) at scale ϵ. We note that

$$R_\epsilon(X,d) \subseteq R_{\epsilon'}(X,d) \quad \text{whenever } \epsilon \leq \epsilon',$$

which is a particular case of the following definition:

Definition 2.15. A filtered simplicial complex $\mathcal{K} = \{K_\epsilon\}_{\epsilon\in\mathbb{R}}$ is a collection of simplicial complexes K_ϵ such that

$$K_\epsilon \subseteq K_{\epsilon'}$$

whenever $\epsilon \leq \epsilon'$. We refer to $\mathcal{K}$ as a filtration.

We note that the family

$$\mathcal{R}(X, d) = \{R_\epsilon(X, d)\}_{\epsilon\in\mathbb{R}}$$

is a filtered complex in the sense of Definition 2.15, called the *Rips filtration* of the metric space (X, d). The main idea behind persistent homology is to track the evolution of homology classes in a filtration as ϵ changes. For instance, as ϵ increases one may see several connected components (0-cycles) merge into one, or an empty spherical cavity (a 2-cycle) become filled. The resulting multiscale summary is recorded in the persistence diagram of the following persistence module.

Definition 2.16. Let $\mathcal{K} = \{K_\epsilon\}_{\epsilon\in\mathbb{R}}$ be a filtration. For each $n \in \mathbb{N}$, define the n-th persistence module

$$H_n(\mathcal{K}; \mathbb{F}) = \{H_n(K_\epsilon; \mathbb{F}),\ T_{\epsilon,\epsilon'} : H_n(K_\epsilon; \mathbb{F}) \to H_n(K_{\epsilon'}; \mathbb{F}), \epsilon \leq \epsilon'\}$$

as the family of $\mathbb{F}$-vector spaces $H_n(K_\epsilon; \mathbb{F})$ and linear transformations $T_{\epsilon,\epsilon'}$ induced by the inclusion maps $K_\epsilon \hookrightarrow K_{\epsilon'}$, for $\epsilon \leq \epsilon'$. The n-th persistent homology groups are

$$H_n^{\epsilon,\epsilon'}(\mathcal{K}; \mathbb{F}) = \mathrm{im}(T_{\epsilon,\epsilon'})$$

and their dimensions over $\mathbb{F}$ are the persistent Betti numbers

$$\beta_n^{\epsilon,\epsilon'}(\mathcal{K}; \mathbb{F}) := \mathrm{rank}(T_{\epsilon,\epsilon'}) = \dim_{\mathbb{F}}(H_n^{\epsilon,\epsilon'}(\mathcal{K}; \mathbb{F})).$$

If $\mathcal{K} = \{K_\epsilon\}_{\epsilon\in\mathbb{R}}$ and $n \in \mathbb{N}$ are such that $H_n(\mathcal{K}; \mathbb{F})$ is pointwise finite dimensional, then Definition 2.7 ensures the existence of the barcode

$$\mathrm{bcd}_n(\mathcal{K}) = \mathrm{bcd}(H_n(\mathcal{K}; \mathbb{F}))$$

and the persistence diagram $\mathrm{dgm}_n(\mathcal{K}) = \mathrm{dgm}(H_n(\mathcal{K}; \mathbb{F}))$.

Remark 2. When the n-th homology of a filtration changes at only finitely many filtration values, the resulting persistence diagram has a particularly simple description in terms of persistent Betti numbers; see [Cohen-Steiner et al. 2007, p. 106]. Indeed, let $\mathcal{K} = \{K_\epsilon\}_{\epsilon\in\mathbb{R}}$ be a filtration whose n-th persistence module is pointwise finite and changes at only finitely many values of ϵ, namely $\epsilon_1 < \epsilon_2 < \cdots < \epsilon_J$ (i.e., finitely many homological critical values). Then given interleaved values $\epsilon_j < r_j < \epsilon_{j+1}$ with $r_0 = \epsilon_{-1} = -\infty$ and $r_{J+1} = \epsilon_{J+1} = \infty$, the persistence diagram $\mathrm{dgm}_n(\mathcal{K})$ is the collection of points (ϵ_i, ϵ_j) that have *positive* multiplicity

$$\beta_n^{r_{i-1},r_j}(\mathcal{K}; \mathbb{F}) - \beta_n^{r_i,r_j}(\mathcal{K}; \mathbb{F}) + \beta_n^{r_i,r_{j-1}}(\mathcal{K}; \mathbb{F}) - \beta_n^{r_{i-1},r_{j-1}}(\mathcal{K}; \mathbb{F}). \tag{1}$$

Unless otherwise stated, we assume that every metric space (X, d) is finite. Hence for each $\epsilon \in \mathbb{R}$ the Rips complex $R_\epsilon(X, d)$ is a finite simplicial complex and the persistence module

$$H_n(\mathcal{R}(X, d); \mathbb{F})$$

is pointwise finite. The corresponding barcode and persistence diagram are denoted by $\mathrm{bcd}_n^R(X, d)$ and $\mathrm{dgm}_n^R(X, d)$, respectively, and the intervals $I \in \mathrm{bcd}_n^R(X, d)$ are closed on the left and open on the right. An interval $[a, b) \in \mathrm{bcd}_n^R(X, d)$ indicates that an n-cycle is born at $\epsilon = a$ and becomes trivial at $\epsilon = b$; its persistence (lifetime) $b - a$ provides a measure of robustness for this homological feature. Plotting $\mathrm{dgm}_n^R(X, d)$ in the extended plane $\overline{\mathbb{R}}^2$ yields a visualization of the persistent homology of the Rips filtration $\mathcal{R}(X, d)$. Points $(a, b) \in \mathrm{dgm}_n^R(X, d)$ that lie far from the diagonal $y = x$ represent topological features of (X, d) with greater robustness, as the stability theorem (Theorem 2.19, which we describe next) implies.

When working with metric spaces and the Rips filtration, we can connect the bottleneck distance of the corresponding persistence diagrams with the Gromov–Hausdorff distance. The latter measures the similarity between bounded metric spaces and is defined below.

Definition 2.17. Given two nonempty bounded subsets A and B of a metric space (X, d), the *Hausdorff distance* $d_H(A, B)$ is defined as

$$d_H(A, B) = \max\Big\{\sup_{a\in A}\inf_{b\in B} d(a, b), \sup_{b\in B}\inf_{a\in A} d(b, a)\Big\},$$

where $d(a, b)$ denotes the distance between points a and b in X.

Definition 2.18. For two bounded metric spaces (X_1, d_1) and (X_2, d_2), the Gromov–Hausdorff distance

$$d_{GH}(X_1, X_2)$$

is defined as follows. Take any common metric space Z and any pair of isometric embeddings $\phi_1 : X_1 \to Z$ and $\phi_2 : X_2 \to Z$; compute the Hausdorff distance between $\phi_1(X_1)$ and $\phi_2(X_2)$ in Z. Then $d_{GH}(X_1, X_2)$ is the infimum of all such Hausdorff distances:

$$d_{GH}(X_1, X_2) = \inf_{Z,\phi_1,\phi_2} d_H(\phi_1(X_1), \phi_2(X_2)).$$

The aforementioned connection is the content of the well-known Rips stability theorem [Cohen-Steiner et al. 2007; Chazal et al. 2016].

Theorem 2.19. *Let X_1 and X_2 be finite metric spaces. Then*

$$d_B(\mathrm{dgm}_n^R(X_1, d_1), \mathrm{dgm}_n^R(X_2, d_2)) \le 2d_{GH}(X_1, X_2).$$

In addition to stability, one can also describe the Rips persistence of metric products.

Definition 2.20. Let (X, d_X) and (Y, d_Y) be metric spaces. The maximum metric d_∞ is given by

$$d_\infty((x, y), (x', y')) = \max\{d_X(x, x'), d_Y(y, y')\},$$

where $(x, y), (x', y') \in X \times Y$.

We note that $(X \times Y, d_\infty)$ is a metric space. Further, its barcodes are given by [Gakhar and Perea 2019]:

Theorem 2.21 (persistent Künneth formula). *Let (X, d_X) and (Y, d_Y) be finite metric spaces. Then,*

$$\mathrm{bcd}_n^R(X \times Y, d_\infty) = \bigcup_{i+j=n} \{I \cap J \mid I \in \mathrm{bcd}_i^R(X, d_X),\ J \in \mathrm{bcd}_j^R(Y, d_Y)\},$$

for all $n \in \mathbb{N}$.

Finally, we present an observation which we use repeatedly:

Proposition 2.22. *Let (X, d_X) and (Y, d_Y) be two finite metric spaces. Suppose there exists a bijection $f : X \to Y$ such that for some $\lambda > 0$*

$$d_X(t_1, t_2) = \lambda d_Y(f(t_1), f(t_2)).$$

Then

$$\mathrm{dgm}_n^R(X, d_X) = \{(\lambda a, \lambda b) \mid (a, b) \in \mathrm{dgm}_n^R(Y, d_Y)\}.$$

Proof. Let us define the metric $d_Y^\lambda = \lambda d_Y$ on Y. By assumption, f is an isometry between (X, d_X) and (Y, d_Y^λ). This implies that f induces simplicial isomorphisms between $R_\epsilon(X, d_X)$ and $R_\epsilon(Y, d_Y^\lambda)$ for all $\epsilon \geq 0$. This, in turn, induces isomorphisms on the corresponding persistence modules, which implies they have the same persistence diagrams. □

2.2. ***Dynamical systems.*** Having presented persistent homology as a tool to measure shape in discrete data, we now introduce the framework that models the source of said data. Indeed, several real-world scientific measurements arise from underlying deterministic mechanisms. Although said mechanism may be unknown or highly complex, the theory of dynamical systems enables its mathematical description. The framework consists of a phase space M that represents all of the relevant states of the system and a function Φ that keeps track of the evolution of the system. The following definitions are taken from [Perea 2019].

Definition 2.23. A global continuous time dynamical system is a pair (M, Φ), where M is a topological space and $\Phi : \mathbb{R} \times M \to M$ is a continuous map such that $\Phi(0, p) = p$, and $\Phi(s, \Phi(t, p)) = \Phi(s + t, p)$ for all $p \in M$ and all $t, s \in \mathbb{R}$.

Note that any autonomous system of ordinary differential equations

$$\dot{x}(t) = \Lambda(x(t)), \quad x(t) \in M,$$

on a smooth manifold M defines a dynamical system. Its flow $\Phi_t : M \to M$ is given by following the integral curves (solutions) of the ODE from each initial condition. Hence the evolution of the system is fully determined by the vector field Λ and the chosen initial state.

Representing a model in this fashion allows for a topological understanding of the system. This is done by looking at trajectories in the phase space M; indeed, although most systems can only be solved numerically, given equations, a general understanding of the shape of trajectories in M provides qualitative information of the system [Skraba et al. 2012]. In particular, knowing the topology of an *attractor* — i.e., a subset of M that pulls nearby trajectories into it — is of great significance. Formally:

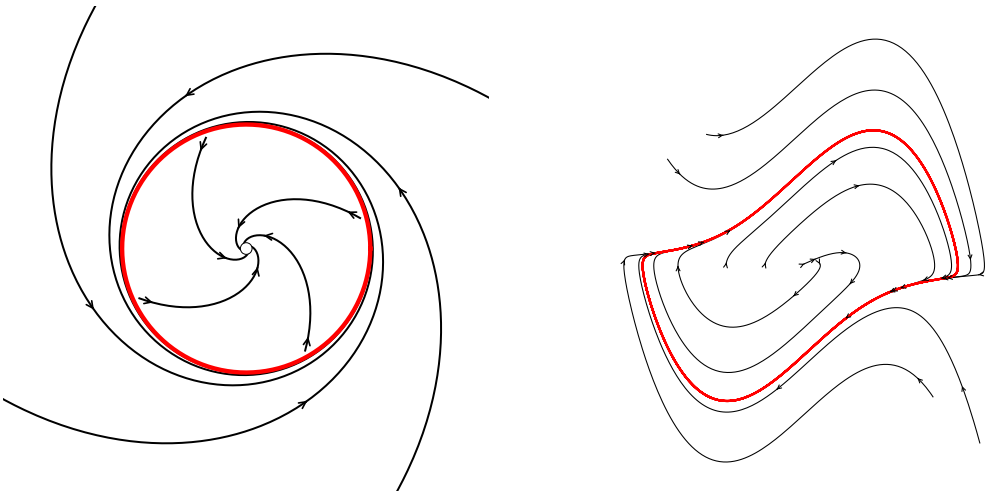

Figure 4. Trajectories of the system from Example 2.25, plotted in the xy-plane (left) and from Example 2.26 in the $x\dot{x}$ plane (right). In each case, the attractor is a topological circle, highlighted in red.

Definition 2.24. A set $A \subseteq M$ is called an attractor if

(1) it is compact,

(2) it is an invariant set, i.e., if $a \in A$ then $\Phi(t, a) \in A$ for all $t \geq 0$,

(3) there is an invariant open neighborhood U of A such that $A = \bigcap_{t \geq 0} \{\Phi(t, p) \mid p \in U\}$.

Example 2.25. Consider the dynamical system given by the radial equation (in polar coordinates)

$$\dot{r} = r(1 - r^2), \quad \dot{\theta} = 1,$$

where $r \geq 0$. This system has a circle as an attractor in the xy-plane, shown in red in Figure 4, left.

Example 2.26. Consider the van der Pol equation

$$\ddot{x} + \mu(x^2 - 1)\dot{x} + x = 0,$$

where $\mu \geq 0$ is a parameter. This system also has an attractor in the $x\dot{x}$-plane as shown in Figure 4, right. In this case, it is not a round unit circle, yet it is topologically equivalent to it.

An attractor that is homeomorphic to a circle corresponds to a system exhibiting periodicity. In general, an attractor that is homeomorphic to an N-dimensional torus, a toroidal attractor, comes from a quasiperiodic system [Gakhar and Perea 2024]. In practice, we often only have a measurement of the dynamical system in the form of time-series data. The underlying equations governing the system are unknown — i.e., neither M nor Φ are given. Nevertheless, there is a way to reconstruct attractors of this unknown system while preserving qualitative information. Concretely, Takens' landmark theorem [1981] shows that a single time series measurement — sampled from a generic observation function — suffices to reconstruct the topology of the underlying attractor.

Theorem 2.27 (Takens' embedding). *Let M be an m-dimensional compact Riemannian manifold. For pairs $(\phi, \bar{f})$, where $\phi \in C^2(M, M)$ and $\bar{f} \in C^2(M, \mathbb{R})$, it is a generic property that the following map is an embedding*:

$$\Psi_{\phi,\bar{f}} : M \to \mathbb{R}^{2m+1}, \quad \Psi_{\phi,\bar{f}}(p) = \left(\bar{f}(p), \bar{f}(\phi(p)), \bar{f}(\phi^2(p)), \ldots, \bar{f}(\phi^{2m}(p))\right)$$

The reconstruction given by the image of $\Psi_{\phi,\bar{f}}$ may look different from the original state space M, but we are assured it will be topologically equivalent. This is a powerful guarantee that validates the *sliding-window embedding* (defined below) as a means to reconstruct observed dynamics from time-series data.

Definition 2.28. For a function $f : \mathbb{R} \to \mathbb{C}$, an integer $d > 0$ called the embedding dimension, and a real number $\tau > 0$ called the time delay, the sliding-window embedding of f at t is given by

$$\mathrm{SW}_{d,\tau} f(t) = \begin{bmatrix} f(t) \\ f(t+\tau) \\ \vdots \\ f(t+d\tau) \end{bmatrix} \in \mathbb{C}^{d+1}.$$

For $T \subseteq \mathbb{R}$ a set of time points, the sliding-window point cloud of f sampled at T is the set

$$\mathbb{SW}_{d,\tau}(T) = \{\mathrm{SW}_{d,\tau} f(t) \mid t \in T\}.$$

In the context of a dynamical system $\Phi : \mathbb{R} \times M \to M$, an observation function $\bar{f} : M \to \mathbb{R}$, and an initial condition $p_0 \in M$ such that the trajectory $t \mapsto \Phi(t, p_0)$ densely samples an attractor $A \subseteq M$, Takens' theorem implies that the sliding window of the time series $t \mapsto \bar{f} \circ \Phi(t, p_0)$ — with appropriate parameters $\tau > 0$ and $d \geq \dim(M)$ — produces a point cloud whose Rips persistence diagrams can be used to infer the homology of A.

In particular, for toroidal attractors and selecting (d, τ) according to [Gakhar and Perea 2024], we are detecting homological features of an N-dimensional torus, as depicted in Figures 3 and 5. In summary, here are steps for detecting the presence of toroidal attractors given time-series data:

(1) Start with a time series pertaining to a measurement of a system.

(2) Construct the sliding-window point cloud from it.

(3) Compute its persistence diagrams to determine if the point cloud samples an N-torus.

Although sliding windows and persistence are well established and have found multiple applications [Tralie and Perea 2018; Perea et al. 2015; Gakhar and Perea 2019], computing persistence diagrams remains computationally taxing. We now move onto the tools that will enable the fast approximation of Rips persistence diagrams of sliding-window point clouds from quasiperiodic functions.

2.3. *Fourier analysis of quasiperiodic signals.*

Definition 2.29. We say that $f : \mathbb{R} \to \mathbb{C}$ is quasiperiodic with frequency vector $\omega = (\omega_1, \ldots, \omega_N)$ if $\{\omega_i\}_{i=1}^N$ are positive real numbers which are linearly independent over $\mathbb{Q}$ (i.e., incommensurate) and

$$f(t) = F(\omega_1 t, \ldots, \omega_N t),$$

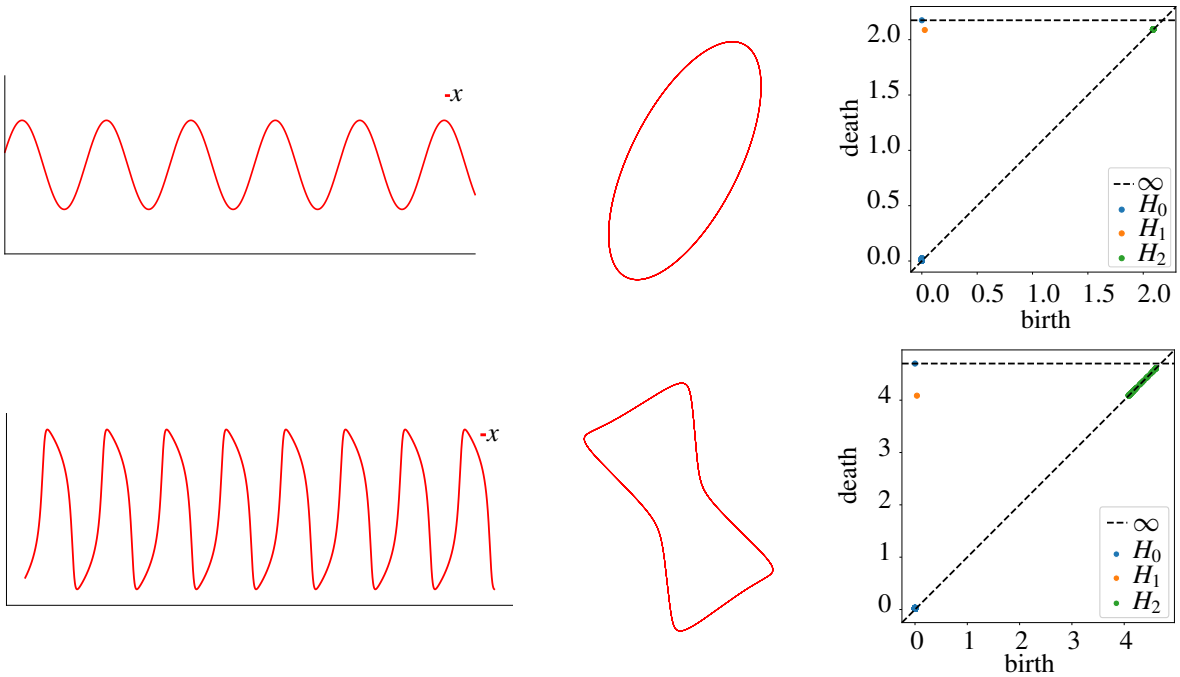

Figure 5. Left column: the $x(t)$ coordinate of the solution to the radial system from Example 2.25 (top row) and the van der Pol system from Example 2.26 (bottom row). Middle column: the sliding-window embedding of $x(t)$ with appropriate parameters d and τ. Right column: the Rips persistence diagrams in dimensions 0, 1 and 2 for the sliding-window point cloud.

where $F : \mathbb{T}^N \to \mathbb{C}$ is a complex-valued continuous function on the N-torus $\mathbb{T}^N = \mathbb{R}^N/\mathbb{Z}^N$, called the parent function of f.

As we will see below, one can leverage the spectrum of a quasiperiodic function to infer the underlying frequency vector, as well as to approximate the Rips persistence diagrams of the sliding-window point cloud. This is enabled by the following result [Gakhar and Perea 2024, Theorem 1.7 and Corollary 1.13].

Theorem 2.30. *Let $f : \mathbb{R} \to \mathbb{C}$ be a quasiperiodic function with frequency vector $\boldsymbol{\omega}$ and parent function F. For each $\boldsymbol{k} \in \mathbb{Z}^N$, the $\boldsymbol{k}$-th Fourier coefficient of F can be computed as*

$$\widehat{F}(\boldsymbol{k}) = \lim_{\lambda \to \infty} \frac{2\pi}{\lambda} \int_0^{\lambda} f(t) e^{-2\pi i \langle \boldsymbol{k}, t\boldsymbol{\omega} \rangle} \, dt,$$

where $i = \sqrt{-1}$. Furthermore, if

$$S_K f(t) = \sum_{\|\boldsymbol{k}\|_\infty \leq K} \widehat{F}(\boldsymbol{k}) e^{2\pi i \langle \boldsymbol{k}, t\boldsymbol{\omega} \rangle} \quad \text{for } K \in \mathbb{N}$$

then for each $j, T \in \mathbb{N}$, $\mathrm{dgm}_j^R(\mathbb{SW}_{d,\tau} f(T))$ can be approximated in bottleneck distance by

$$\mathrm{dgm}_j^R(\mathbb{SW}_{d,\tau} S_K f(T))$$

as $K \to \infty$. The approximation is of order $O(K^{N/2-r})$ when $|\widehat{F}(\boldsymbol{k})| = O(\|\boldsymbol{k}\|_2^{-r})$ and $r > \frac{1}{2}N$.

Theorem 2.30 shows that, in bottleneck distance, the Rips persistence diagrams of a quasiperiodic signal f can be arbitrarily closely approximated by those of its truncated Fourier series $S_K f(t)$. Moreover, the coefficients of $S_K f$ are determined by the spectrum of f, which can be estimated via the discrete Fourier transform (implemented in the FFT algorithm).

This result justifies reducing general quasiperiodic functions to finite exponential sums of the form

$$f(t) = \sum_{j=1}^{M} c_j e^{2\pi i \omega_j t} \quad \text{for } M \in \mathbb{N},\ c_j \in \mathbb{C} \setminus \{0\} \text{ and } \omega_j \in \mathbb{R},$$

where $\omega_1, \ldots, \omega_M$ are not necessarily $\mathbb{Q}$-linearly independent. Set $\tilde{c}_j = \sqrt{d+1}c_j$, choose an embedding dimension $d \in \mathbb{N}$ and a delay $\tau > 0$, and let

$$A = \frac{1}{\sqrt{d+1}} \begin{pmatrix} 1 & \cdots & 1 \\ e^{2\pi i \omega_1 \tau} & \cdots & e^{2\pi i \omega_M \tau} \\ \vdots & \ddots & \vdots \\ e^{2\pi i \omega_1 d\tau} & \cdots & e^{2\pi i \omega_M d\tau} \end{pmatrix} \in \mathbb{C}^{(d+1)\times M} \quad \text{and} \quad v_t = \begin{pmatrix} \tilde{c}_1 e^{2\pi i \omega_1 t} \\ \vdots \\ \tilde{c}_M e^{2\pi i \omega_M t} \end{pmatrix} \in \mathbb{C}^M.$$

In this setting, the sliding-window embedding can be written succinctly as

$$\mathrm{SW}_{d,\tau} f(t) = A v_t,$$

and according to [Gakhar and Perea 2024, Corollary 1.3], the set $\{v_t\}_{t\in\mathbb{R}}$ is a dense subset of a space homeomorphic to the N-torus, for $N \leq M$ equal to the dimension of $\mathrm{span}_{\mathbb{Q}}\{\omega_1, \ldots, \omega_M\}$ as a $\mathbb{Q}$-vector space. The multidimensional version of Kronecker's approximation theorem, as presented in [Hlawka et al. 1991, Chapter 2, Theorem 2], allows one to take $t \in \mathbb{N}$ and retain density. Furthermore, d and τ can be chosen so that the same holds true for $\{\mathrm{SW}_{d,\tau} f(t)\}_{t\in\mathbb{N}}$ [Gakhar and Perea 2024, Theorem 1.15].

With this in mind, the Cartesian product

$$G_T = \prod_{j=1}^{M} \{\tilde{c}_j e^{2\pi i \omega_j t} \mid t = 0, 1, \ldots, T\} \tag{2}$$

offers a way to approximate $\{v_t\}_{t=0}^{T}$ in Hausdorff distance, and hence the resulting Rips persistence diagrams in bottleneck distance, by Theorem 2.19, as $T \to \infty$. See also Figure 10. This is useful since the persistence diagrams of G_T can be readily computed using the persistent Künneth formula (Theorem 2.21). We will show in Theorem 4.3 that this approach can be used to approximate the Rips persistence diagrams of the sliding-window embedding of f.

2.4. ***Continued fraction expansion.*** The continued-fraction expansion of a real number lies at the heart of our work. All definitions, propositions, and theorems in this section are classical and can be found in standard references — most notably [Olds 1963, Chapter 3], and for Theorem 2.38 see, e.g., [Rockett and Szüsz 1992, p. 22]. As we will show, continued-fraction data enables us to infer persistent-homology

information of sliding-window point clouds once the frequencies of the signal are estimated — e.g., with the FFT.

Definition 2.31. Let ω be a real number. The continued-fraction expansion of ω is given by

$$\omega = a_1 + \cfrac{1}{a_2 + \cfrac{1}{a_3 + \cfrac{1}{a_4 + \cdots}}} := [a_1, a_2, a_3, \dots],$$

where $a_1 \in \mathbb{Z}$ and $a_k \in \mathbb{N}$, for $k > 1$.

Note that the expansion, which is obtained by repeated applications of the division algorithm, is infinite if and only if ω is irrational. From here onward, we let ω denote a positive irrational number.

Definition 2.32. Let $k \in \mathbb{N}$. The k-th convergent of ω is given by

$$\frac{p_k}{q_k} = [a_1, a_2, \dots, a_k] \in \mathbb{Q}.$$

The terms p_k and q_k play a special role in the theory, and can be obtained recursively as follows.

Proposition 2.33. *The numerator p_k and the denominator q_k of the k-th convergent of ω satisfy*

$$p_k = a_k p_{k-1} + p_{k-2} \quad \text{and} \quad q_k = a_k q_{k-1} + q_{k-2},$$

for $k \geq 1$, where

$$p_0 = 1, \quad q_0 = 0, \quad p_{-1} = 0, \quad q_{-1} = 1.$$

Proposition 2.33 provides a convenient computational method for obtaining the k-th convergent of ω, and implies the following result.

Proposition 2.34. *The terms p_k and q_k are relatively prime.*

We can quantify the quality of the convergent p_k/q_k as an approximation to ω by examining the absolute error

$$\left| \omega - \frac{p_k}{q_k} \right|.$$

Proposition 2.35. *Let $k \geq 1$. Then*

$$\frac{1}{2q_k q_{k+1}} < \left| \omega - \frac{p_k}{q_k} \right| < \frac{1}{q_k q_{k+1}} < \frac{1}{q_k^2}.$$

Furthermore, this result allows us to establish the existence and uniqueness of infinite continued-fraction expansions. Indeed, this follows by noting that $q_k < q_{k+1}$ for all $k \geq 1$, and justifies the equality sign in Definition 2.31. The next result further characterizes their convergence behavior.

Proposition 2.36. *Let $k \geq 1$ be odd. Then*

$$\frac{p_k}{q_k} < \omega < \frac{p_{k+1}}{q_{k+1}}.$$

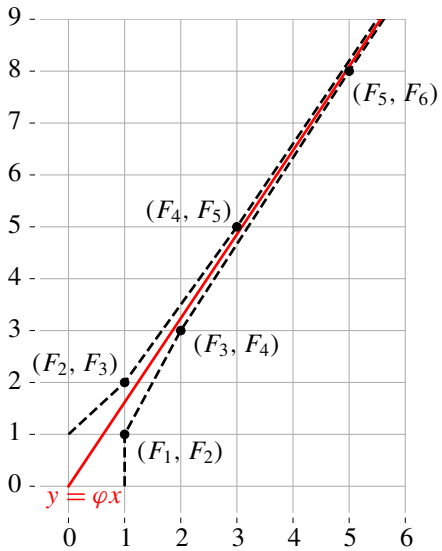

Figure 6. The Klein diagram for the golden ratio $\varphi = \frac{1}{2}(1+\sqrt{5})$. Here F_k denotes the k-th Fibonacci number, which can be used to compute the k-th convergent p_k/q_k of φ; specifically, $p_k/q_k = F_k/F_{k-1}$.

Example 2.37. The results presented here can be used to argue that the golden ration φ is the "most" irrational number. Indeed, by computing

$$\varphi = \tfrac{1}{2}(1+\sqrt{5}) = 1 + \cfrac{1}{1+\cfrac{1}{1+\cfrac{1}{1+\cdots}}} = [1, 1, 1, \cdots],$$

one can show that this expression corresponds to the slowest possible rate of convergence. The Klein diagram shown in Figure 6 provides a geometric picture of this observation.

We end this section by stating a critical property of the k-th convergent of ω attributed to Lagrange. Namely, that the k-th convergent provides a best rational approximation with bounded denominator to ω; see [Rockett and Szüsz 1992, p. 22].

Theorem 2.38. *Let a/b be different from p_{k+1}/q_{k+1} with $0 < b \leq q_{k+1}$. Then*

$$|b\omega - a| \geq |q_k\omega - p_k| > |q_{k+1}\omega - p_{k+1}|.$$

2.5. ***The three-gap theorem method.*** Thus far we have shown that exponential functions are fundamental in the study of quasiperiodic signals, and that their frequencies can be optimally approximated with their k-th convergents. If we let

$$f(t) = e^{2\pi i\omega t},$$

then viewed as a map $f : \mathbb{R} \to S^1 \subseteq \mathbb{C}$, $f(t)$ parametrizes the unit circle. Fix a natural number $T \in \mathbb{N}$ and consider the times $t = 0, 1, \ldots, T$. This yields the sample

$$\{f(t) \mid t = 0, 1, \ldots, T\} = \{e^{2\pi i\omega t} \mid t = 0, 1, \ldots, T\},$$

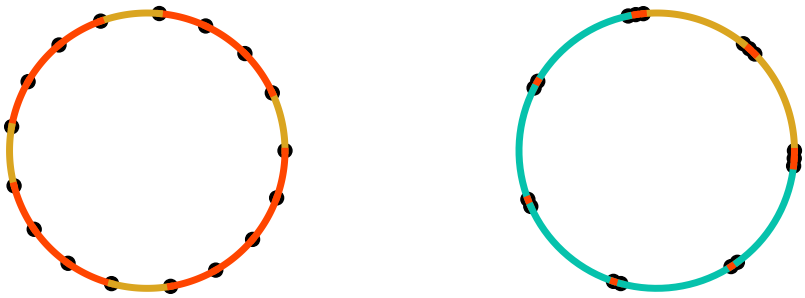

Figure 7. On the left, we depict $S_{\pi-1,17}$ in black. Each gap size is shown in a different color; in this case, there are only two distinct gaps (red and yellow). On the right, we show $S_{\sqrt{5},17}$ in black, which has three distinct gap sizes (green, red and yellow).

which in flat coordinates (i.e., modulo 1), corresponds to

$$\{t\omega \mod 1 \mid t = 0, 1, \ldots, T\} \subseteq [0, 1].$$

Definition 2.39. For any real number $x \in \mathbb{R}$, write

$$[x] = x \mod 1$$

for its equivalence class on the flat circle $[0, 1]/0 \sim 1$. For $T \in \mathbb{N}$ and $\omega \in \mathbb{R} \setminus \mathbb{Q}$ we let

$$S_{\omega,T} := \{[0], [\omega], [2\omega], \ldots, [T\omega]\}.$$

By identifying the endpoints of $[0, 1]$, we view $S_{\omega,T}$ as a finite sequence of points on the circle (see Figure 7). To measure distances in this space we use the quotient metric

$$\bar{d}([x], [y]) = \min\{|x - y|, |1 - (y - x)|, |1 - (x - y)|\},$$

which turns $(S_{\omega,T}, \bar{d})$ into a metric space. When we write $S_{\omega,T}$ we will require $\omega \in \mathbb{R} \setminus \mathbb{Q}$ unless otherwise stated. The asymptotic sampling properties of this set are well documented [Zhigljavsky and Aliev 1999] and follow in large part from the three-gap theorem (Steinhaus conjecture) [van Ravenstein 1988], which we state below.

Theorem 2.40 (three-gap theorem). *Let $T \in \mathbb{N}$ and $\omega \in \mathbb{R} \setminus \mathbb{Q}$. The points in $S_{\omega,T}$ partition $[0, 1]/0 \sim 1$ into $T + 1$ intervals, such that their lengths take at least two and at most three different values. If three distinct lengths occur — denoted in increasing order by δ_A, δ_B and δ_C — then*

$$\delta_C = \delta_A + \delta_B.$$

Importantly, the conclusion of the three-gap theorem — that there are at most three distinct interval lengths — holds for every irrational ω and every sample size T. We illustrate the content of the three gap theorem in Figure 7 for $\omega = \pi - 1$ (left), $\omega = \sqrt{5}$ (right) and $T = 17$.

The lengths δ_A, δ_B and δ_C in the three gap theorem are in fact governed by the convergents of ω [Leong 2017]; see Proposition 3.2 for explicit formulas for the gaps and their multiplicities. This observation yields

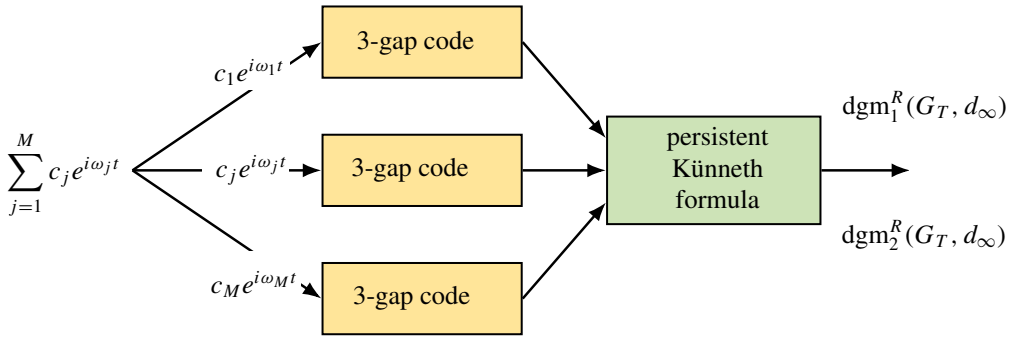

Figure 8. A schematic representation of the 3G method. Starting from a sum of exponentials approximating a quasiperiodic function, we extract its frequency parameters via the FFT. We then apply the three gap construction independently to each frequency circle and compute the resulting persistence diagrams. Finally, we assemble these individual diagrams using the persistent Künneth formula, yielding an approximation to the Rips persistence of the sliding-window point cloud of the original signal.

a complete description of pairwise distances between neighboring points in $S_{\omega,T}$, and we will show in the next section how they can be used to compute the persistence diagrams of the Rips filtration $\mathcal{R}(S_\omega, \bar{d})$; see Figure 9 for an example. This leads to our approximation scheme for the persistence diagrams of sliding-window point clouds from quasiperiodic functions: The three-gap theorem method (3G), depicted schematically in Figure 8.

In short, we first extract the independent frequencies ω_j of the input quasiperiodic signal; then, for each frequency ω_j, we compute its continued-fraction expansion and use its convergents to find the lengths δ_A and δ_B (and $\delta_C = \delta_A + \delta_B$ when appropriate) in $(S_{\omega_j,T}, \bar{d})$, as well as their multiplicities (see Proposition 3.2); the lengths and multiplicities of these gaps are used to derive the barcodes $\mathrm{bcd}_n^R(S_{\omega_j,T}, \bar{d})$ and persistence diagrams $\mathrm{dgm}_n^R(S_{\omega_j,T}, \bar{d})$ — this is the content of Corollaries 3.4 and 3.8, and the output of Algorithm 1 below; finally, we use the persistent Künneth theorem to compute $\mathrm{dgm}_n^R(G_T, d_\infty)$ — see (2) for the definition of G_T and Theorem 4.5 for the results. The quality of the approximation of $\mathrm{dgm}_n^R(\mathbb{SW}_{d,\tau} f(T), d_2)$ via $\mathrm{dgm}_n^R(G_T, d_\infty)$ is discussed in detail in Section 4, for d_2 the standard Euclidean distance in $\mathbb{C}^{d+1}$. The relevant approximation results are given in Theorem 4.3 and further clarified in Remark 3.

1: Input frequency ω_j
2: Scale frequency $\omega_j = \omega_j/(2\pi)$
3: Obtain continued-fraction expansion, C.F.E., of ω_j
4: Use C.F.E. as shown in Proposition 3.2 to obtain gaps and their multiplicities
5: Scale gaps as detailed in Theorem 4.5 to obtain the barcode of $\mathcal{R}(S_{\omega_j,T}, \bar{d})$

Algorithm 1. 3-Gap code.

3. Main results

We now move on to detailing the connection between the three-gap theorem and persistence diagrams. The theorem allows us to compute persistence diagrams by leveraging information from the continued-fraction expansion of the underlying frequencies estimated with the FFT of a quasiperiodic signal. With this at hand, we show how, using the persistent Künneth formula, we can establish an approximation method for the persistence diagrams of sliding-window embeddings from quasiperiodic functions. Finally, we show how to obtain error bounds for our method.

3.1. ***Persistence diagrams.*** Computing $\mathrm{dgm}_0^R(S_{\omega,T}, \bar{d})$ via the three-gap theorem reduces to relating the lengths of the gaps to the convergents of ω. Although the connection between gap sizes and convergents is classical (see [van Ravenstein 1988; Beresnevich and Leong 2017]), we include an alternative proof of the three-gap theorem that highlights how each continued-fraction coefficient contributes to the 0-th persistence diagram. Throughout, let $\{0, 1, \ldots, T\} \subseteq \mathbb{N}$ denote the (discrete) set of time values, and let $\omega \in \mathbb{R} \setminus \mathbb{Q}$ be an irrational frequency. We begin by finding the distance from a point in $S_{\omega,T}$ to its nearest neighbor:

$$\mathrm{Cl}(j) = \min\left\{\bar{d}([j\omega], x) \mid x \in S_{\omega,T} \setminus \{[j\omega]\}\right\} \quad \text{for } 0 \le j \le T.$$

Lemma 3.1. *Let $T \in \mathbb{N}$ and $\omega \in \mathbb{R} \setminus \mathbb{Q}$ with i-th convergent p_i/q_i. Fix $0 \le j_0 \le T$ and let*

$$\bar{k}(j_0) = \max\{j \mid q_j \le \max\{j_0, T - j_0\}\}.$$

If $0 \le j_1 \le T$ satisfies

$$|j_0 - j_1| = q_{\bar{k}(j_0)},$$

then

$$\mathrm{Cl}(j_0) = \bar{d}([j_0\omega], [j_1\omega]).$$

Proof. Let us first show the result when $j_0 = 0$. In this case, $\mathrm{Cl}(j_0) = \bar{d}([j_0\omega], [j_1\omega])$ if and only if

$$[j_1\omega] = \min\{[j\omega], 1 - [j\omega] \mid 1 \le j \le T\}.$$

The latter is equivalent to finding $p \in \mathbb{N}$ such that for all $p_0, q_0 \in \mathbb{N}$ with $q_0 \le T$,

$$|j_1\omega - p| \le |q_0\omega - p_0|.$$

By Theorem 2.38 this is satisfied by the convergents of ω, namely by $j_1 = q_{\bar{k}(0)}$ and $p = p_{\bar{k}(0)}$. This shows the result for $j_0 = 0$. For the general case, we note that since

$$\bar{d}([j_0\omega], [j_1\omega]) = \bar{d}(0, [|j_0 - j_1|\omega]),$$

we can apply the previous argument, now restricting $p_0 \le \max\{j_0, T - j_0\}$ since $|j_0 - j_1| \le \max\{j_0, T - j_0\}$. Similarly, the minimum is achieved when $|j_0 - j_1| = q_{\bar{k}_j(j_0)}$, and the result follows. □

Proposition 3.2. *Let $T \in \mathbb{N}$ and $\omega \in \mathbb{R} \setminus \mathbb{Q}$ with continued-fraction expansion $[a_1, a_2, a_3, \dots]$ and i-th convergent p_i/q_i, and arrange the elements of $S_{\omega,T} = \{[0], [\omega], \dots, [T\omega]\}$ in increasing order as*

$$[n_i\omega] < [n_{i+1}\omega] \quad \text{for } 0 \leq i < T.$$

Let k, r and s be the unique integers for which

$$q_k + q_{k-1} \leq T < q_k + q_{k+1} \qquad \text{and} \qquad T = rq_k + q_{k-1} + s \quad \text{for } 1 \leq r \leq a_{k+1} \text{ and } 0 \leq s \leq q_k - 1,$$

and let $D_i = q_i\omega - p_i$ for each i. If

$$\delta_A = |D_k|, \quad \delta_B = |D_{k+1}| + (a_{k+1} - r)|D_k|, \quad \delta_C = \delta_A + \delta_B,$$

and $\oplus$ denotes addition modulo $T+1$, then for $0 \leq i \leq T$,

$$\{\bar{d}([n_i\omega], [n_{i\oplus 1}\omega])\} \subseteq \{\delta_A, \delta_B, \delta_C\}.$$

Furthermore, denoting the multiplicity of gaps by $N_I = \#\{i \mid \bar{d}([n_i\omega], [n_{i\oplus 1}\omega]) = \delta_I\}$, we have

$$N_A = T + 1 - q_k, \quad N_B = s + 1, \quad N_C = q_k - s - 1.$$

Proof. We first establish the existence and uniqueness of k, r and s. For all $i \geq 0$,

$$q_i + q_{i-1} < q_i + q_{i+1}.$$

Thus $T \in [q_k + q_{k-1}, q_k + q_{k+1})$ for some k; that this k is unique follows by the monotonicity of $\{q_i + q_{i-1}\}_i$. We also note that by assumption $T - q_{k-1} \geq q_k$; thus by the division algorithm there exist unique r and s such that

$$T - q_{k-1} = rq_k + s,$$

where $1 \leq r$ and $0 \leq s \leq q_k$. On the other hand, since $T - q_{k-1} < q_k + q_{k+1} - q_{k-1} = (a_{k+1} + 1)q_k$, by Proposition 2.33, we conclude $r \leq a_{k+1}$. This shows the existence and uniqueness of k, r and s.

For convenience of presentation in what follows, we define the notion of the "right" and "left" of a point. For $x, y \in S_{\omega,T}$, we say that y is to the right of x if $\bar{d}(x, y)$ is achieved by traversing from x clockwise to y in this representation. Similarly, achieving the distance while traversing counterclockwise is used to define left. Since translation is an isometry under $\bar{d}$ we note $[i_1\omega]$ is to the right or left of $[i_2\omega]$ if and only if for all $j \geq 0$, $[(i_1 + j)\omega]$ is to the right or left, respectively, of $[(i_2 + j)\omega]$. We make use of this fact repeatedly.

Let us now show that

$$\{\bar{d}(0, [n_1\omega]), \bar{d}(0, [n_T\omega])\} = \{\delta_A, \delta_B\}.$$

This equality will apply to general points in $S_{\omega,T}$ by the isometry property of the translation map. In particular, it will allow us to compute N_A and N_B, and find the explicit pairs that achieve the corresponding gap. We assume without loss of generality that

$$[q_k\omega] \leq \tfrac{1}{2},$$

i.e., $[q_k\omega]$ is to the right of 0. By Proposition 2.36, $[q_{k-1}\omega]$ and $[q_{k+1}\omega]$ are to the left of 0, i.e., $[q_k\omega] < [q_{k-1}\omega], [q_{k+1}\omega]$. Thus by Lemma 3.1 $n_1 = q_k$, and thus

$$\bar{d}(0, [n_1\omega]) = [q_k\omega] = \delta_A.$$

In fact, Lemma 3.1 also shows

$$[q_k\omega] < [q_{k-1}\omega] < [q_{k+1}\omega].$$

Moreover, since

$$\bar{d}([q_{k-1}\omega], [(q_{k-1}+q_k)\omega]) = \bar{d}([q_k\omega], 0) = [q_k\omega]$$

and, by Theorem 2.38,

$$\bar{d}([q_k\omega], 0) < \bar{d}([q_{k-1}\omega], 0),$$

we conclude

$$[q_{k-1}\omega] < [(q_{k-1}+q_k)\omega].$$

Repeating this argument and noting $q_{k+1} = a_{k+1}q_k + q_{k-1}$ we can say that for $0 \le i \le a_{k+1}$,

$$[q_{k-1}\omega] \le [(q_{k-1}+iq_k)\omega] \le [(q_{k-1}+(i+1)q_k)\omega] \le [q_{k+1}\omega].$$

Thus

$$\begin{aligned}\bar{d}([(q_{k-1}+iq_k)\omega], 0) &= \bar{d}([q_{k+1}\omega], 0) + \sum_{j=0}^{a_{k+1}-i-1} \bar{d}([(q_{k-1}+jq_k)\omega], [(q_{k-1}+(j+1)q_k)\omega]) \\ &= |D_{k+1}| + (a_{k+1}-i)|D_k|.\end{aligned}$$

By Lemma 3.1 we can conclude $n_T = q_{k-1} + rq_k$ and the above computation shows

$$\bar{d}([(q_{k-1}+rq_k)\omega], 0) = |D_{k+1}| + (a_{k+1}-r)|D_k| = \delta_B.$$

Thus we have shown

$$\{\bar{d}(0, [n_1\omega]), \bar{d}(0, [n_T\omega])\} = \{\delta_A, \delta_B\}.$$

Now consider $n_j \in [0, (r-1)q_k + q_{k-1} + s]$. Since $n_j + q_k \le T$ and

$$\bar{d}([n_j\omega], [(n_j+q_k)\omega]) = \bar{d}([q_k\omega], 0) = [q_k\omega] = \delta_A,$$

we conclude, by the same reasoning as with $n_j = 0$, that $[(n_j+q_k)\omega]$ is the closest point to the right of $[n_j\omega]$, i.e., $n_{j\oplus 1} = n_j + q_k$. This shows there are

$$(r-1)q_k + q_{k-1} + s + 1 = (rq_k + q_{k-1} + s) + 1 - q_k = T + 1 - q_k$$

different gaps of length δ_A, i.e., $N_A = T + 1 - q_k$.

Similarly, for $n_j \in [rq_k + q_{k-1}, T]$ we note

$$n_j - (rq_k + q_{k-1}) \in [0, s],$$

and thus

$$\bar{d}([n_j\omega], [(n_j - (rq_k + q_{k-1}))\omega]) = \bar{d}([(rq_k + q_{k-1})\omega], 0) = |D_{k+1}| + (a_{k+1}-r)|D_k| = \delta_B.$$

Carrying over the arguments for the case $n_j = rq_k + q_{k-1}$, we conclude $[(n_j - (rq_k + q_{k-1}))\omega]$ is the closest point to the left of $[n_j\omega]$, i.e., $n_{j-1} = n_j - (rq_k + q_{k-1})$. Thus there are $s+1$ different gaps of length δ_B, i.e., $N_B = s+1$.

What remains to consider is the case $n_j \in ((r-1)q_k + q_{k-1} + s, rq_k + q_{k-1})$. If $r > 1$, we note

$$\bar{d}([n_j\omega], [(n_j - q_k)\omega]) = \bar{d}([q_k\omega], 0) = [q_k\omega] = \delta_A.$$

Thus $n_{j-1} = n_j - q_k$. Since $n_j - q_k < (r-1)q_k + q_{k-1} + s$, we have already accounted for this gap. On the other hand,

$$\bar{d}([n_j\omega], [n_{j\oplus 1}\omega]) \neq \delta_A, \delta_B$$

since $n_j + q_k, n_j + (rq_k + q_{k-1}) > T$. As a consequence of the inequality shown before,

$$[q_{k-1}\omega] \leq [(q_{k-1} + iq_k)\omega] \leq [(q_{k-1} + (i+1)q_k)\omega] \leq [q_{k+1}\omega],$$

we conclude the next smallest gap length is

$$|D_{k+1}| + (a_{k+1} - (r-1))|D_k| = |D_{k+1}| + (a_{k+1} - r + 1)|D_k| = \delta_A + \delta_B = \delta_C.$$

This gap is achieved when $n_{j+1} = n_j - ((r-1)q_k + q_{k-1})$. Thus there are $q_k - s - 1$ different gaps of length δ_C, i.e., $N_C = q_k - s - 1$.

We have shown there are distinct gaps, distances between adjacent points, of lengths δ_A, δ_B and δ_C. Furthermore, since

$$N_A + N_B + N_C = T + 1,$$

we conclude all gaps have been accounted for, i.e.,

$$\{\bar{d}([n_i\omega], [n_{i\oplus 1}\omega])\} \subseteq \{\delta_A, \delta_B, \delta_C\}. \qquad \square$$

It is clear that the three-gap theorem follows from Proposition 3.2. Furthermore, Proposition 3.2 details the relation between the length of the gaps and the k-th convergents of ω. The next theorem translates what this means in terms of the 0-th dimensional persistence diagram of $S_{\omega,T}$. We assume $r < a_{k+1}$ and $s+1 < p_k$ to streamline the exposition; the other parameter regimes lead to analogous conclusions:

- Case: $r \geq a_{k+1}$. In this regime one shows that $\delta_A > \delta_B$. In Theorem 3.3 below, one then swaps the labels δ_A and δ_B so that the combinatorial pattern of gap lengths remains identical.
- Case: $s+1 \geq p_k$. Here $N_C = 0$, meaning no third gap appears. Equivalently, the final merge of adjacent points occurs at $\epsilon = \max\{\delta_A, \delta_B\}$, which then plays the role of δ_C in the theorem's description.

In each scenario, relabeling or omitting the appropriate gap lengths shows that the proof of Theorem 3.3 carries over without change.

Theorem 3.3. *Let $T \in \mathbb{N}$ and $\omega \in \mathbb{R} \setminus \mathbb{Q}$ with continued-fraction expansion $[a_1, a_2, a_3, \dots]$ and i-th convergent p_i/q_i, and let k, r and s be the unique integers for which*

$$q_k + q_{k-1} \le T < q_k + q_{k+1} \qquad \text{and} \qquad T = rq_k + q_{k-1} + s \quad \text{for } 1 \le r \le a_{k+1} \text{ and } 0 \le s \le q_k - 1.$$

Let

$$D_i = q_i\omega - p_i,$$

and suppose

$$r < a_{k+1} \quad \text{and} \quad s + 1 < p_k.$$

Then

$$H_0(R_\epsilon(S_{\omega,T}, \bar{d}); \mathbb{F}) = \begin{cases} \mathbb{F}^{T+1} & \text{if } 0 \le \epsilon < |D_k|, \\ \mathbb{F}^{q_k} & \text{if } |D_k| \le \epsilon < |D_{k+1}| + (a_{k+1} - r)|D_k|, \\ \mathbb{F}^{q_k - s - 1} & \text{if } |D_{k+1}| + (a_{k+1} - r)|D_k| \le \epsilon < |D_{k+1}| + (a_{k+1} - r + 1)|D_k|, \\ \mathbb{F} & \text{if } |D_{k+1}| + (a_{k+1} - r + 1)|D_k| \le \epsilon. \end{cases}$$

Proof. Let δ_I and N_I, where $I \in \{A, B, C\}$, be as defined in Proposition 3.2. Since $r < a_{k+1}$ we note $\bar{k}(T) = k$, and thus by Lemma 3.1,

$$\delta_A < \delta_B.$$

Furthermore, since $s + 1 < q_k$, there are three possible lengths for the gaps, i.e., $N_C > 0$.

At $\epsilon = 0$,

$$H_0(R_0(S_{\omega,T}, \bar{d}); \mathbb{F}) = \mathbb{F}^{T+1}$$

by definition. We can interpret this as connected components that are separated by $N_A + N_B + N_C = T + 1$ gaps. Since the Rips complex connects two points when ϵ is greater or equal to their distance, the first time points will be connected is at $\epsilon = \delta_A$. Now, the newly formed connected components will be separated from each other only at the gaps of length δ_B and δ_C, i.e.,

$$H_0(R_{\delta_A}(S_{\omega,T}, \bar{d}); \mathbb{F}) = \mathbb{F}^{N_B + N_C} = \mathbb{F}^{q_k}.$$

Similarly, the next time we connect points is at $\epsilon = \delta_B$; now the remaining connected components will be separated by only N_C gaps, and thus

$$H_0(R_{\delta_B}(S_{\omega,T}, \bar{d}); \mathbb{F}) = \mathbb{F}^{N_C} = \mathbb{F}^{q_k - s - 1}.$$

The last time we connected points was at δ_C; since this means all adjacent points are connected we conclude there is only one connected component, i.e.,

$$H_0(R_{\delta_C}(S_{\omega,T}, \bar{d}); \mathbb{F}) = \mathbb{F}. \qquad \square$$

Corollary 3.4. *Let $T \in \mathbb{N}$ and $\omega \in \mathbb{R} \setminus \mathbb{Q}$ with continued-fraction expansion $[a_1, a_2, a_3, \dots]$ and i-th convergent p_i/q_i, and let k, r and s be the unique integers for which*

$$q_k + q_{k-1} \le T < q_k + q_{k+1} \qquad \text{and} \qquad T = rq_k + q_{k-1} + s \quad \text{for } 1 \le r \le a_{k+1} \text{ and } 0 \le s \le q_k - 1.$$

Let

$$D_i = q_i\omega - p_i,$$

and suppose

$$r < a_{k+1} \quad \textit{and} \quad s+1 < p_k.$$

If

$$\delta_A = |D_k|, \quad \delta_B = |D_{k+1}| + (a_{k+1} - r)|D_k|, \quad \delta_C = \delta_A + \delta_B,$$

then

$$\mathrm{dgm}_0^R(S_{\omega,T}, \bar{d}) = \{(0, \delta_A)^{T+1-q_k}, (0, \delta_B)^{s+1}, (0, \delta_C)^{q_k-s-2}, (0, \infty)\},$$

where the upper indices indicate the multiplicity of each point in the diagram.

Proof. For $\epsilon \leq \epsilon'$ let

$$T_{\epsilon,\epsilon'} : H_0(R_\epsilon(S_{\omega,T}, \bar{d}); \mathbb{F}) \to H_0(R_{\epsilon'}(S_{\omega,T}, \bar{d}); \mathbb{F})$$

denote the linear transformation induced by the inclusion of Rips complexes, and let $\beta_0^{\epsilon,\epsilon'}$ be its rank. Since $S_{\omega,T}$ is the vertex set of $R_\epsilon(S_{\omega,T}, \bar{d})$ for all $\epsilon \geq 0$, and a basis for $H_0(K; \mathbb{F})$ is given by choosing a vertex in each path-connected component of the simplicial complex K, then $T_{\epsilon,\epsilon'}$ is surjective whenever $0 \leq \epsilon \leq \epsilon'$, and the zero map for $\epsilon < 0$. Hence $\beta_0^{\epsilon,\epsilon'}$ is equal to 0 if $\epsilon < 0$, and equal to $\dim_{\mathbb{F}}(H_0(R_{\epsilon'}(S_{\omega,T}, \bar{d}); \mathbb{F}))$ if $0 \leq \epsilon \leq \epsilon'$. The result follows from applying Corollary 3.4 to compute $\dim_{\mathbb{F}}(H_0(R_{\epsilon'}(S_{\omega,T}, \bar{d}); \mathbb{F}))$, and combining the result with the formula from (1); see Remark 2. □

Example 3.5. Consider the parameter value $\sqrt{5}$ shown in Figure 9, top left. To compute the lengths of the gaps in $S_{\sqrt{5},16}$, we follow Proposition 3.2. We note that

$$\sqrt{5} = [2, 4, 4, 4, 4, 4, \dots],$$

and thus using Proposition 2.33 we obtain $q_1 = 1$, $q_2 = 4$, $q_3 = 17$ and $q_4 = 72$. Since

$$q_1 + q_2 \leq 16 < q_2 + q_3$$

we conclude $k = 2$. One can readily check that

$$16 = 3q_2 + q_1 + 3$$

is the desired decomposition, i.e., $r = 3$ and $s = 3$. Hence we have $N_A = 16 + 1 - 4 = 13$ gaps of length $\delta_A = |4\sqrt{5} - 9| \approx 0.05573$, $N_B = 3 + 1 = 4$ gaps of length $\delta_B = |17\sqrt{5} - 38| + (4-3)|4\sqrt{5} - 9| \approx 0.06888$, and $N_C = 4 - 3 - 1 = 0$ gaps of length $\delta_C = |17\sqrt{5} - 38| + (4 - 3 + 1)|4\sqrt{5} - 9| \approx 0.12461$. Thus, by using Corollary 3.4 in the case of two gaps, we have

$$\mathrm{dgm}_0^R(S_{\sqrt{5},16}, \bar{d}) = \{(0, 0.05573)^{13}, (0, 0.06888)^3, (0, \infty)\}.$$

Example 3.6. Similarly, we consider the set $S_{\pi-1,16}$ shown in Figure 9, bottom left. In this case

$$\pi - 1 = [2, 7, 15, 292, 1, 1, \dots],$$

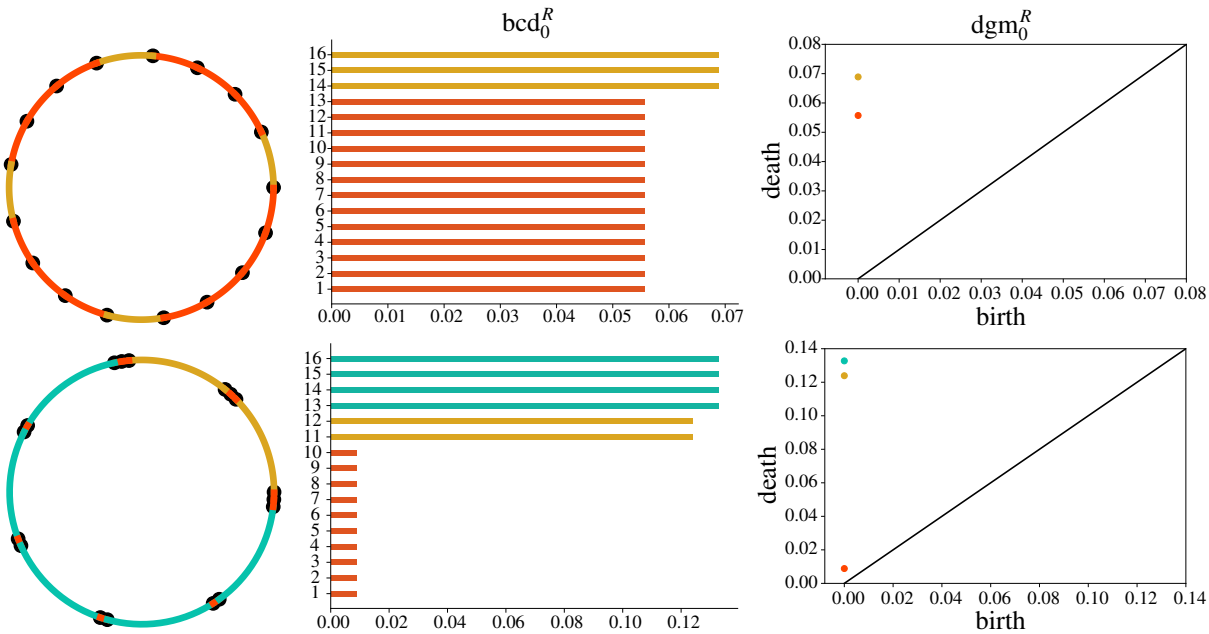

Figure 9. We illustrate above how the 0-th dimensional persistent homology can be computed using the three-gap theorem. At $\epsilon = 0$, all points in $(S_{\omega,T}, \bar{d})$ count as a basis in $H_0(R_\epsilon(S_{\omega,T}, \bar{d}); \mathbb{F})$ (birth time). At $\epsilon = \delta_A$, points get connected for the first time. The three possible gaps are the only instances when components are connected (death time). Top row: the set $S_{\sqrt{5},16}$ is illustrated with the two gaps it creates. These can be traced in the barcodes and persistent diagram as shown. Bottom row: the set $S_{\pi-1,16}$ creates three gaps.

$p_1 = 1$, $p_2 = 7$, $p_3 = 106$ and $p_4 = 113$. Thus $k = 2$ since

$$p_1 + p_2 \leq 16 < p_2 + p_3.$$

Furthermore, the desired decomposition is given by

$$16 = 2p_2 + p_1 + 1,$$

i.e., $r = 2$ and $s = 1$. Thus we have $N_A = 16+1-7 = 10$ gaps of length $\delta_A = |7(\pi-1)-15| \approx 0.00885$, $N_B = 2$ gaps of length $\delta_B = |106(\pi-1)-227|+(15-2)|7(\pi-1)-15| \approx 0.12389$, and $N_C = 7-1-1 = 5$ gaps of length $\delta_C = |106(\pi-1)-227|+(15-2+1)|7(\pi-1)-15| \approx 0.13274$. Moreover, by Corollary 3.4

$$\mathrm{dgm}_0^R(S_{\pi-1,16}, \bar{d}) = \{(0, 0.00885)^{10}, (0, 0.12389)^2, (0, 0.13274)^4, (0, \infty)\}.$$

We also compute $\mathrm{dgm}_1^R(S_{\omega,T}, \bar{d})$. In Theorem 3.7 we assume

$$s + 1 < q_k \quad \text{and} \quad \delta_C < \tfrac{1}{3}$$

to simplify the presentation. If instead $s + 1 \geq q_k$, then $N_C = 0$ and only the two gap lengths δ_A and δ_B occur — so one may simply set $\max\{\delta_A, \delta_B\}$ in place of δ_C. Likewise, if the largest gap δ_M satisfies

$\delta_M \geq \frac{1}{3}$, then by Lemma A.5 we have $\lambda \leq \delta_M$, forcing every potential 1-cycle to be 0 in H_1, i.e., a trivial case. We denote addition modulo $T+1$ by $\oplus$.

Theorem 3.7. *Let $T \in \mathbb{N}$ and $\omega \in \mathbb{R} \setminus \mathbb{Q}$ with continued-fraction expansion $[a_1, a_2, a_3, \dots]$ and i-th convergent p_i/q_i, and let k, r and s be the unique integers for which*

$$q_k + q_{k-1} \leq T < q_k + q_{k+1} \qquad \text{and} \qquad T = rq_k + q_{k-1} + s \quad \text{for } 1 \leq r \leq a_{k+1} \text{ and } 0 \leq s \leq q_k - 1.$$

Let

$$D_i = q_i\omega - p_i,$$

and assume

$$s + 1 < q_k \quad \text{and} \quad |D_{k+1}| + (a_{k+1} - r + 1)|D_k| < \tfrac{1}{3}.$$

Let Γ be the set containing the pairs (x, y) for $x, y \in S_{\omega,T}$ and $x < y$, for which there exists a $z \in ([0, x) \cup (y, 1)) \cap S_{\omega,T}$ such that $1 - \bar{d}(x, y) \leq 2\max\{\bar{d}(y, z), \bar{d}(x, z)\} \leq 2\bar{d}(x, y)$. If

$$\lambda = \min\{\bar{d}(x, y) \mid (x, y) \in \Gamma\},$$

then

$$H_1(R_\epsilon(S_{\omega,T}, \bar{d}); \mathbb{F}) = \begin{cases} \mathbb{F} & \text{if } |D_{k+1}| + (a_{k+1} - r + 1)|D_k| \leq \epsilon < \lambda, \\ 0 & \text{otherwise.} \end{cases}$$

Proof. Let $\{x_i\}_{i=0}^{T}$ be the points of $S_{\omega,T}$ in ascending order, and consider the 1-chain

$$\sigma = \sum_{i=0}^{T} \{x_i, x_{i\oplus 1}\},$$

where $i \oplus 1$ denotes $i + 1 \mod (T+1)$. By Proposition 3.2, the maximum distance between consecutive points is

$$\delta_C = |D_{k+1}| + (a_{k+1} - r + 1)|D_k|.$$

Hence

$$\sigma \in C_1(R_\epsilon(S_{\omega,T}, \bar{d})) \iff \epsilon \geq \delta_C.$$

One checks immediately that $\partial\sigma = 0$. Lemma A.4 then shows any nonboundary 1-cycle in

$$C_1(R_{\delta_C}(S_{\omega,T}, \bar{d}))$$

is homologous to σ. Consequently $[\sigma]$ generates $H_1(R_{\delta_C}(S_{\omega,T}, \bar{d}); \mathbb{F})$.

To show that σ is not a boundary, it suffices to prove there is no 2-simplex $\tau \in C_2(R_{\delta_C}(S_{\omega,T}, \bar{d}))$ with $\partial\tau = \sigma$. We argue by contradiction. Suppose there exists $\tau \in C_2(R_{\delta_C}(S_{\omega,T}, \bar{d}))$ such that $\partial\tau = \sigma$. Let us first show we may assume, without loss of generality, that

$$\bar{d}(0, x_1) = \delta_C.$$

To see this, we construct an explicit isometry on $(S_{\omega,T}, \bar{d})$ which reindexes the points accordingly. By hypothesis, there is an index i_0 with

$$\bar{d}(x_{i_0}, x_{i_0 \oplus 1}) = \delta_C.$$

Define

$$\phi(x_i) = \begin{cases} x_i - x_{i_0} & \text{if } i \geq i_0, \\ 1 - (x_{i_0} - x_i) & \text{if } i < i_0. \end{cases}$$

A direct check shows

$$\bar{d}(\phi(x_i), \phi(x_j)) = \bar{d}(x_i, x_j) \quad \text{for all } i, j,$$

so ϕ is an isometry. By Proposition 2.22, it induces identical persistence diagrams. Finally, set

$$y_j = \phi(x_{i_0 \oplus j}) \quad \text{for } j = 0, 1, \ldots, T,$$

so that

$$0 = y_0 < y_1 < \cdots < y_T < 1 \quad \text{and} \quad \bar{d}(y_0, y_1) = \delta_C.$$

This relabeled sequence $\{y_j\}$ therefore has the desired property; we thereafter write $x_j := y_j$ for all j.

Now, since $\partial\tau = \sigma$, τ must contain a 2-simplex of the form $\{0, x_1, x_{i_0}\}$ for some $i_0 > 1$. If $x_{i_0} \leq \frac{1}{2}$, then

$$\bar{d}(0, x_{i_0}) = \bar{d}(0, x_1) + \bar{d}(x_1, x_{i_0}) > \delta_C.$$

If instead $x_{i_0} > \frac{1}{2}$ and $\bar{d}(x_1, x_{i_0}) \leq \delta_C$, then

$$\bar{d}(0, x_{i_0}) = \min\{\bar{d}(0, x_1) + \bar{d}(x_1, x_{i_0}), 1 - [\bar{d}(0, x_1) + \bar{d}(x_1, x_{i_0})]\} > \delta_C,$$

since $\delta_C < \frac{1}{3}$. In either case $\{0, x_1, x_{i_0}\} \notin \tau$, contradicting $\partial\tau = \sigma$. Therefore no such τ exists, and σ is not a boundary.

To conclude the proof, it suffices to show that for any ϵ with $\delta_C < \epsilon \leq \lambda$, a 2-simplex

$$\tau \in C_2(R_\epsilon(S_{\omega,T}, \bar{d}))$$

satisfying $\partial\tau = \sigma$ appears precisely at $\epsilon = \lambda$. In particular, no such τ exists when $\epsilon < \lambda$, but at $\epsilon = \lambda$ one does. Hence for all $\epsilon \geq \lambda$, the class $[\sigma]$ is trivial in $H_1(R_\epsilon(S_{\omega,T}, \bar{d}); \mathbb{F})$.

We now demonstrate by explicit construction that at $\epsilon = \lambda$ there is a 2-chain $\tau \in C_2(R_\lambda(S_{\omega,T}, \bar{d}))$ with $\partial\tau = \sigma$. Choose $(x_{n_1}, x_{n_2}) \in \Gamma$ so that $\lambda = \bar{d}(x_{n_1}, x_{n_2})$, and let x_{n_3} be the third point paired with (x_{n_1}, x_{n_2}). By assumption

$$\max\{\bar{d}(x_{n_2}, x_{n_3}), \bar{d}(x_{n_1}, x_{n_3})\} \leq \bar{d}(x_{n_2}, x_{n_3}) = \lambda.$$

Hence $\{x_{n_1}, x_{n_2}, x_{n_3}\}$ lies in $R_\lambda(S_{\omega,T}, \bar{d})$.

Next define the 2-chain

$$\tau_1 = \sum_{i=n_1}^{n_2-1} \{x_i, x_{i+1}, x_{n_2}\}.$$

Because for $n_1 \leq i < n_2$,

$$\bar{d}(x_i, x_{i+1}) < \bar{d}(x_{n_1}, x_{n_2}),$$

$\tau_1 \in C_2(R_\lambda(S_{\omega,T}, \bar{d}))$.

To define the analogous chains τ_2 and τ_3, we use the fact that $S_{\omega,T}$ can be identified with the circle. Let $\{x_i^2\}_{i=1}^{A_2}$ be the sequence of points obtained by starting at x_{n_2} and moving clockwise until x_{n_3}, inclusive — so $x_1^2 = x_{n_2}$ and $x_{A_2}^2 = x_{n_3}$. We then set

$$\tau_2 = \sum_{i=1}^{A_2-1} \{x_i^2, x_{i+1}^2, x_{n_3}\},$$

interpreting $\tau_2 = 0$ if $A_2 = 2$.

Similarly, let $\{x_i^3\}_{i=1}^{A_3}$ be the sequence of points starting at x_{n_3} and moving clockwise until x_{n_1}, with $x_1^3 = x_{n_3}$ and $x_{A_3}^3 = x_{n_1}$. We define

$$\tau_3 = \sum_{i=1}^{A_3-1} \{x_i^3, x_{i+1}^3, x_{n_1}\},$$

again taking $\tau_3 = 0$ if $A_3 = 2$. In all cases, each τ_j lies in $C_2(R_\lambda(S_{\omega,T}, \bar{d}))$.

Finally set

$$\tau = \tau_1 + \tau_2 + \tau_3 + \{x_{n_1}, x_{n_2}, x_{n_3}\}.$$

By construction $\tau \in C_2(R_\lambda(S_{\omega,T}, \bar{d}))$, and one checks directly that $\partial\tau = \sigma$. This completes the existence argument at $\epsilon = \lambda$.

To complete the proof, let $\epsilon \in (\delta_C, \lambda)$. If one assumes the existence of a 2-simplex $\tau_0 \in C_2(R_\epsilon(S_{\omega,T}, \bar{d}))$ with $\partial\tau_0 = \sigma$, then by considering

$$\max\{\bar{d}(x, y), \bar{d}(y, z), \bar{d}(z, x) \mid \{x, y, z\} \in \tau_0\}$$

one obtains a contradiction to the minimality of λ; see Lemma A.5. □

Corollary 3.8. *Let $T \in \mathbb{N}$ and $\omega \in \mathbb{R} \setminus \mathbb{Q}$ with continued-fraction expansion $[a_1, a_2, a_3, \dots]$ and i-th convergent p_i/q_i, and let k, r and s be the unique integers for which*

$$q_k + q_{k-1} \le T < q_k + q_{k+1} \qquad \text{and} \qquad T = rq_k + q_{k-1} + s \quad \text{for } 1 \le r \le a_{k+1} \text{ and } 0 \le s \le q_k - 1.$$

Let

$$D_i = q_i\omega - p_i,$$

and assume

$$s + 1 < q_k \quad \text{and} \quad |D_{k+1}| + (a_{k+1} - r + 1)|D_k| < \tfrac{1}{3}.$$

Let Γ be the set containing the pairs (x, y) for $x, y \in S_{\omega,T}$ and $x < y$, for which there exists a $z \in ([0, x) \cup (y, 1)) \cap S_{\omega,T}$ such that $1 - \bar{d}(x, y) \le 2\max\{\bar{d}(y, z), \bar{d}(x, z)\} \le 2\bar{d}(x, y)$. If

$$\lambda = \min\{\bar{d}(x, y) \mid (x, y) \in \Gamma\},$$

then

$$\mathrm{dgm}_1^R(S_{\omega,T}, \bar{d}) = \{(|D_{k+1}| + (a_{k+1} - r + 1)|D_k|, \lambda)\}.$$

Proof. The 1-cycle σ constructed in the proof of Theorem 3.7 provides a persistent generator for

$$H_1(R_\epsilon(S_{\omega,T}, \bar{d}); \mathbb{F})$$

whenever $|D_{k+1}| + (a_{k+1} - r + 1)|D_k| = \delta_C \leq \epsilon < \lambda$. This shows that the persistent Betti numbers $\beta_1^{\epsilon,\epsilon'}$ are zero for $\epsilon < \delta_C$ or $\lambda \leq \epsilon'$, and equal to one for $\delta_C \leq \epsilon \leq \epsilon' < \lambda$. The result follows from Remark 2. □

4. Approximation method

We now detail our approximation method for the sliding-window embedding of quasiperiodic functions. To handle general quasiperiodic functions, it is sufficient to consider those that are sums of exponentials, as discussed in Section 2.3. When f takes this form, its sliding-window embedding admits the matrix representation

$$\mathrm{SW}_{d,\tau} f(t) = A v_t.$$

Recall that

$$\mathbb{SW}_{d,\tau} f(T) = \{\mathrm{SW}_{d,\tau} f(t) \mid t = 0, \ldots, T\}$$

denotes the corresponding sliding-window point cloud, and let ϕ_T be the trajectory $\{v_t \mid t = 0, \ldots, T\}$; we assume $T' \leq T$, and let G_T be as defined in (2). Throughout this section let $l_0, M, N \in \mathbb{N}$, we use j and l as dummy variables, and we let $i = \sqrt{-1} \in \mathbb{C}$. Our approximation method relates the following metric spaces, and their corresponding persistence diagrams:

$$(\mathbb{SW}_{d,\tau} f(T), d_2) \sim (\phi_T, d_\infty) \sim (G_{T'}, d_\infty).$$

The first relation is obtained using an eigenvalue argument. Let $\sigma_{\min}$ and $\sigma_{\max}$ be the smallest and largest singular values of A, respectively.

Lemma 4.1. *Let*

$$f(t) = \sum_{j=1}^{M} c_j e^{2\pi i \omega_j t} \quad \textit{for } c_j \in \mathbb{C} \setminus \{0\} \textit{ and } \omega_j \in \mathbb{R}.$$

Define $k = \max\{\sigma_{\min}^{-1}, \sigma_{\max}\sqrt{M}\}$. *Suppose* $(a_1, b_1) \in \mathrm{dgm}_{l_0}^R(\phi_T, d_\infty)$. *If*

$$\frac{b_1}{a_1} > k^2,$$

then there exists a unique $(a_0, b_0) \in \mathrm{dgm}_{l_0}^R(\mathbb{SW}_{d,\tau} f(T), d_2)$ *such that*

$$\frac{1}{k} < \frac{\max\{b_0, b_1\}}{\min\{b_0, b_1\}}, \frac{\max\{a_0, a_1\}}{\min\{a_0, a_1\}} < k.$$

Proof. Note that

$$\sigma_{\min} d_2(v_{t_1}, v_{t_2}) \leq d_2(A v_{t_1}, A v_{t_2}) \leq \sigma_{\max} d_2(v_{t_1}, v_{t_2}) \quad \text{and} \quad d_\infty(v_{t_1}, v_{t_2}) \leq d_2(v_{t_1}, v_{t_2}) \leq \sqrt{M} d_\infty(v_{t_1}, v_{t_2}).$$

We conclude that

$$d_\infty(v_{t_1}, v_{t_2}) \leq d_2(v_{t_1}, v_{t_2}) \leq \frac{1}{\sigma_{\min}} d_2(Av_{t_1}, Av_{t_2}) \leq \frac{\sigma_{\max}}{\sigma_{\min}} d_2(Av_{t_1}, Av_{t_2}) \leq \sqrt{M} d_\infty(v_{t_1}, v_{t_2}).$$

Since $\mathrm{SW}_{d,\tau} f(t) = Av_t$ and A is full-rank (provided d and τ are chosen according to [Gakhar and Perea 2024]), then

$$R_\epsilon(\mathbb{SW}_{d,\tau} f(T), d_2) \hookrightarrow R_{\epsilon/\sigma_{\min}}(\phi_T, d_\infty) \hookrightarrow R_{\epsilon(\sigma_{\max}/\sigma_{\min})}(\mathbb{SW}_{d,\tau} f(T), d_2)$$

under the induced simplicial maps obtained from $\mu : \mathbb{SW}_{d,\tau} f(T) \to \phi_T$, $\mu(Av_t) = v_t$ and $\nu : \phi_T \to \mathbb{SW}_{d,\tau} f(T)$, $\nu(v_t) = Av_t$. We have the diagram

$$\begin{array}{ccc} R_\epsilon(\mathbb{SW}_{d,\tau} f(T), d_2) & \xrightarrow{\ \iota\ } & R_{k^2\epsilon}(\mathbb{SW}_{d,\tau} f(T), d_2) \\ & {\scriptstyle\mu}\searrow \quad \nearrow{\scriptstyle\nu} & \\ & R_{k\epsilon}(\phi_T, d_\infty) & \end{array}$$

where ι is the inclusion $R_\epsilon(\mathbb{SW}_{d,\tau} f(T), d_2) \hookrightarrow R_{k^2\epsilon}(\mathbb{SW}_{d,\tau} f(T), d_2)$. Furthermore ι is contiguous to $\nu \circ \mu$; that is, for $\sigma \in R_\epsilon(\mathbb{SW}_{d,\tau} f(T), d_2)$ we have $\iota(\sigma) \cup \nu \circ \mu(\sigma) \in R_{k^2\epsilon}(\mathbb{SW}_{d,\tau} f(T), d_2)$. Hence we obtain a commutative diagram at the level of homology, which we reparametrize in logarithmic scale as

$$\begin{array}{ccc} H_n(R_{\ln(\epsilon)}(\mathbb{SW}_{d,\tau} f(T), d_2); \mathbb{F}) & \xrightarrow{\ \iota_*\ } & H_n(R_{2\ln(k)+\ln(\epsilon)}(\mathbb{SW}_{d,\tau} f(T), d_2); \mathbb{F}) \\ & {\scriptstyle\mu_*}\searrow \quad \nearrow{\scriptstyle\nu_*} & \\ & H_n(R_{\ln(k)+\ln(\epsilon)}(\phi_T, d_\infty); \mathbb{F}) & \end{array}$$

This gives us a $\ln(k)$ interleaving which implies by Theorem 2.9 that, if for $(a_1, b_1) \in \mathrm{dgm}_{l_0}^R(\phi_T, d_\infty)$,

$$\ln(b_1) - \ln(a_1) > 2\ln(k),$$

i.e., $b_1/a_1 > k^2$, there exists a unique $(a_0, b_0) \in \mathrm{dgm}_{l_0}^R(\mathbb{SW}_{d,\tau} f(T), d_2)$ such that

$$|\ln(b_1) - \ln(b_0)| < \ln(k) \quad \text{and} \quad |\ln(a_1) - \ln(a_0)| < \ln(k).$$

This implies

$$-\ln(k) < \ln\left(\frac{\max\{b_0, b_1\}}{\min\{b_0, b_1\}}\right), \ln\left(\frac{\max\{a_0, a_1\}}{\min\{a_0, a_1\}}\right) < \ln(k),$$

from which the result follows. □

To relate the two metric spaces

$$(\phi_T, d_\infty) \quad \text{and} \quad (G_{T'}, d_\infty),$$

we apply Theorem 2.19 together with the definition of the bottleneck distance.

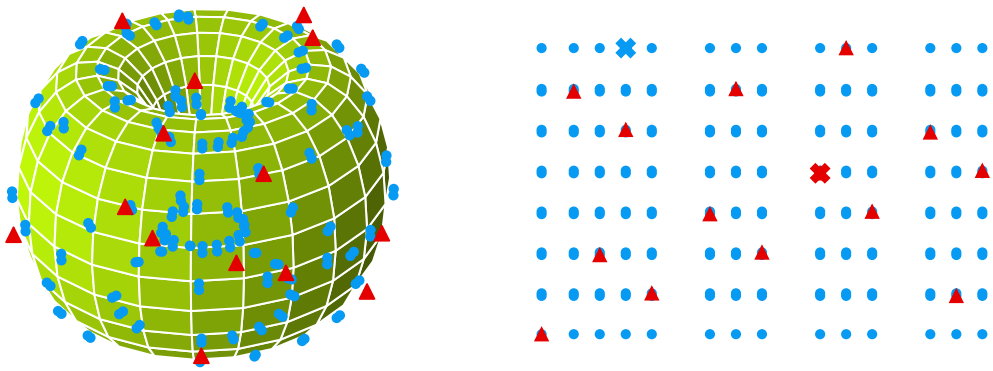

Figure 10. Comparison of ϕ_{13} (red triangles) and G_{13} (blue dots) for a two-frequency torus with incommensurate ω_1 and ω_2. Left: points plotted on the torus $T^2 \subset \mathbb{C}^2$. Right: same points in the rectangular fundamental domain $[0, 1)^2$. The pair marked $\times$ realizes the Hausdorff distance between ϕ_{13} and G_{13}.

Lemma 4.2. *Let* $\lambda = d_{GH}(\phi_T, G_{T'})$ *and* $(a_2, b_2) \in \mathrm{dgm}_{l_0}^R(G_{T'}, d_\infty)$. *If*

$$b_2 - a_2 > 4\lambda,$$

then there exists a unique $(a_1, b_1) \in \mathrm{dgm}_{l_0}^R(\phi_T, d_\infty)$ *such that*

$$|b_1 - b_2| < 2\lambda \quad \textit{and} \quad |a_1 - a_2| < 2\lambda.$$

Proof. Let $B = d_B(\mathrm{dgm}_{l_0}^R(G_{T'}, d_\infty), \mathrm{dgm}_{l_0}^R(\phi_T, d_\infty))$. By Theorem 2.19, $B < 2\lambda$. Thus

$$b_2 - a_2 > 4\lambda > 2B,$$

and hence by the definition of the bottleneck distance, Definition 2.8, there exists a unique $(a_1, b_1) \in \mathrm{dgm}_{l_0}^R(\phi_T, d_\infty)$ such that

$$|b_1 - b_2| < B < 2\lambda \quad \text{and} \quad |a_1 - a_2| < B < 2\lambda, \qquad \square$$

Using the same notation as before, we combine the results to obtain a direct relation between $\mathrm{dgm}_{l_0}^R(\mathbb{SW}_{d,\tau} f(T), d_2)$ and $\mathrm{dgm}_{l_0}^R(G_{T'}, d_\infty)$:

Theorem 4.3. *If* $(a_2, b_2) \in \mathrm{dgm}_{l_0}^R(G_{T'}, d_\infty)$ *satisfies*

$$\frac{b_2 - 2\lambda}{a_2 + 2\lambda} > \max\{k^2, 1\},$$

then there exists a unique $(a_0, b_0) \in \mathrm{dgm}_{l_0}^R(\{\mathrm{SW}_{d,\tau} f(t)\}_{t=0}^T, d_2)$ *satisfying*

$$\max\left\{0, \frac{b_2 - 2\lambda}{k}\right\} \le b_0 \le k(b_2 + 2\lambda) \quad \textit{and} \quad \max\left\{0, \frac{a_2 - 2\lambda}{k}\right\} \le a_0 \le k(a_2 + 2\lambda).$$

Proof. Let us note that the assumption implies

$$b_2 - a_2 > b_2 - a_2 \max\{k^2, 1\} > 2\lambda + 2\lambda \max\{k^2, 1\} > 4\lambda,$$

and thus by Lemma 4.2 there exists a unique $(a_1, b_1) \in \mathrm{dgm}_{l_0}^R(\phi_T, d_\infty)$ such that

$$b_2 - 2\lambda < b_1 < b_2 + 2\lambda \quad \text{and} \quad a_2 - 2\lambda < a_1 < a_2 + 2\lambda.$$

We conclude

$$\frac{b1}{a_1} > \frac{b_2 - 2\lambda}{a_2 + 2\lambda} > k^2,$$

and thus by Lemma 4.1 there exists a unique $(a_0, b_0) \in \mathrm{dgm}_{l_0}^R(\mathbb{SW}_{d,\tau} f(T), d_2)$ such that

$$\frac{1}{k} < \frac{\max\{b_0, b_1\}}{\min\{b_0, b_1\}}, \frac{\max\{a_0, a_1\}}{\min\{a_0, a_1\}} < k.$$

without loss of generality we assume $b_0 = \max\{b_0, b_1\}$. Combining our inequalities, we get

$$\frac{b_2 - 2\lambda}{k} < \frac{b_1}{k} < b_0 < kb_1 < k(b_2 + 2\lambda).$$

An analogous inequality can be obtained for a_0, completing the proof. □

A similar result can be obtained for "symmetric" signals. The following shows it is sufficient to scale our coefficients and consider only half of the frequencies.

Corollary 4.4. *Let*

$$f(t) = \sum_{j=1}^{N} c_j (e^{2\pi i \omega_j t} + e^{-2\pi i \omega_j t}) \quad \textit{for } c_j \in \mathbb{C} \setminus \{0\} \textit{ and } \omega_j \in \mathbb{R}.$$

Let ϕ_T denote the trajectory

$$\phi_T = \{(\tilde{c}_1 e^{2\pi i \omega_1 t}, \ldots, \tilde{c}_N e^{2\pi i \omega_N t})^\top \mid t = 0, 1, \ldots, T\},$$

and let $G_{T'}$ denote the grid

$$G_{T'} = \{(\tilde{c}_1 e^{2\pi i \omega_1 t_1}, \ldots, \tilde{c}_N e^{2\pi i \omega_N t_N})^\top \mid t_n = 0, 1, \ldots, T',\ n = 1, \ldots, N\}.$$

Let $k = \max\{\sigma_{\min}^{-1}, \sigma_{\max}\sqrt{2N}\}$ and $\lambda = d_{GH}(\phi_T, G_{T'})$. If $(a_2, b_2) \in \mathrm{dgm}_{l_0}^R(G_{T'}, d_\infty)$ satisfies

$$\frac{b_2 - 2\lambda}{a_2 + 2\lambda} > \max\{k^2, 1\},$$

then there exists a unique $(a_0, b_0) \in \mathrm{dgm}_{l_0}^R(\mathbb{SW}_{d,\tau} f(T), d_2)$ satisfying

$$\max\left\{0, \frac{b_2 - 2\lambda}{k}\right\} \le b_0 \le k(b_2 + 2\lambda) \quad \textit{and} \quad \max\left\{0, \frac{a_2 - 2\lambda}{k}\right\} \le a_0 \le k(a_2 + 2\lambda).$$

Proof. Let

$$\bar{\phi}_T = \{2^{-\frac{1}{2}}(\tilde{c}_1 e^{2\pi i\omega_1 t}, \ldots, \tilde{c}_N e^{2\pi i\omega_N t}, \tilde{c}_1 e^{-2\pi i\omega_1 t}, \ldots, \tilde{c}_N e^{-2\pi i\omega_N t})^\intercal\}_{0\le t\le T}.$$

By Lemma 4.1, if $(\bar{a}_1, \bar{b}_1) \in \mathrm{dgm}_{l_0}^R(\bar{\phi}_T, d_\infty)$ and

$$\frac{\bar{b}_1}{\bar{a}_1} > k^2,$$

then there exists a unique $(a_0, b_0) \in \mathrm{dgm}_{l_0}^R(\mathbb{SW}_{d,\tau} f(T), d_2)$ such that

$$\frac{1}{k} < \frac{\max\{b_0, \bar{b}_1\}}{\min\{b_0, \bar{b}_1\}}, \frac{\max\{a_0, \bar{a}_1\}}{\min\{a_0, \bar{a}_1\}} < k.$$

On the other hand, since

$$d_2(c_l e^{i\omega_l t_1}, c_l e^{i\omega_l t_2}) = d_2(c_l e^{-i\omega_l t_1}, c_l e^{-i\omega_l t_2}),$$

the maps $\mu : \bar{\phi}_T \to \phi_T$, $\mu(v_t) = \sqrt{2}v_t$ and $\nu : \phi_T \to \bar{\phi}_T$, $\nu(v_t) = 2^{-\frac{1}{2}}v_t$ are isometries. Thus, by Proposition 2.22, $(\bar{a}_1, \bar{b}_1) \in \mathrm{dgm}_{l_0}^R(\bar{\phi}_T, d_\infty)$ if and only if there exist a unique $(a_1, b_1) \in \mathrm{dgm}_{l_0}^R(\phi_T, d_\infty)$ such that

$$a_1 = \bar{a}_1 \quad \text{and} \quad b_1 = \bar{b}_1.$$

Combining this fact with Lemma 4.2, we can say that if $(a_2, b_2) \in \mathrm{dgm}_{l_0}^R(G_{T'}, d_\infty)$ and

$$b_2 - a_2 > 4\lambda,$$

then there exists a unique $(\bar{a}_1, \bar{b}_1) \in \mathrm{dgm}_{l_0}^R(\bar{\phi}_T, d_\infty)$ such that

$$|\bar{b}_1 - b_2| < 2\lambda \quad \text{and} \quad |\bar{a}_1 - a_2| < 2\lambda.$$

By the equivalences that have now been shown, we can replicate the arguments in Theorem 4.3 to conclude the result. □

Remark 3 (error-bound confidence region). Let

$$(a_2, b_2) \in \mathrm{dgm}_{l_0}^R(G_{T'}, d_\infty).$$

Under the hypotheses of Theorem 4.3 there is a corresponding $(a_0, b_0) \in \mathrm{dgm}_{l_0}^R(\mathbb{SW}_{d,\tau} f(T), d_2)$ satisfying

$$\max\left\{0, \frac{b_2 - 2\lambda}{k}\right\} \le b_0 \le k(b_2 + 2\lambda) \quad \text{and} \quad \max\left\{0, \frac{a_2 - 2\lambda}{k}\right\} \le a_0 \le k(a_2 + 2\lambda).$$

It follows that (a_0, b_0) lies in the rectangle

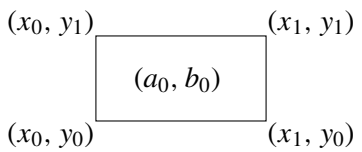

where $x_0 = \max\{0, (a_2 - 2\lambda)/k\}$, $x_1 = k(a_2 + 2\lambda)$, $y_0 = \max\{0, (b_2 - 2\lambda)/k\}$ and $y_1 = k(b_2 + 2\lambda)$. This rectangle serves as a confidence region for the approximation.

We have shown explicitly how $\mathrm{dgm}_{l_0}^R(G_T, d_\infty)$ approximates $\mathrm{dgm}_{l_0}^R(\mathbb{SW}_{d,\tau} f(T), d_2)$. In order to leverage our results from Section 3 we use the Künneth formula; see Theorem 2.21. It allow us to apply Theorems 3.3 and 3.7 to compute $\mathrm{dgm}_{l_0}^R(G_T, d_\infty)$ for $l_0 = 1, 2$. This approach is detailed in the next result. For ease of presentation, we shall express persistence information using the barcode notation bcd_i^R in the following result; these barcodes correspond exactly to the persistence diagrams dgm_i^R as detailed in Section 2.

Theorem 4.5. *Let $c_j \in \mathbb{C}$ and $\omega_j \in \mathbb{R}$. For $a, b, s \in \mathbb{R}$, let $\bar{a} = 2\sin(\pi a)$, $\omega_l' = \omega_l/(2\pi)$ and, for $I = [a, b)$, we let $\bar{I} = [\bar{a}, \bar{b})$ and write sI to denote $[sa, sb)$. Let*

$$G_T = \{(c_1 e^{i\omega_1 t_1}, \ldots, c_N e^{i\omega_N t_N})^\intercal\}_{0 \le t_i \le T}.$$

Then,

$$\mathrm{bcd}_{l_0}^R(G_T, d_\infty) = \bigcup_{\sum_l r_l = l_0} \{|c_1|\bar{I}_1 \cap \cdots \cap |c_N|\bar{I}_N \mid I_l \in \mathrm{bcd}_{r_l}^R(S_{\omega_l', T}, \bar{d})\}.$$

Proof. For $0 \le l \le N$ let

$$X_l = \{c_l e^{i\omega_l t}\}_{t=0}^T.$$

By Theorem 2.21,

$$\mathrm{bcd}_{l_0}^R(G_T, d_\infty) = \bigcup_{\sum_l r_l = l_0} \{J_1 \cap \cdots \cap J_N \mid J_l \in \mathrm{bcd}_{r_l}^R(X_l, d_2)\}.$$

Thus it is sufficient to show that $J_l \in \mathrm{bcd}_{r_l}^R(X_l, d_2)$ if and only if there exists a unique $I_l \in \mathrm{bcd}_{r_l}^R(S_{\omega_l', T'}, \bar{d})$ such that

$$J_l = |c_l|\bar{I}_l.$$

To do so, define $x_j = \omega_l t_j \mod 2\pi$ and consider the metric d_l on X_l given by

$$d_l(c_l e^{i\omega_l t_1}, c_l e^{i\omega_l t_2}) = |c_l| \min\{|x_1 - x_2|, |2\pi - x_2 + x_1|, |2\pi - x_1 + x_2|\}.$$

This metric captures the geodesic distance between points along the circle of radius $|c_l|$ centered at $(0, 0)$. By trigonometric identities,

$$d_2(c_l e^{i\omega_l t_1}, c_l e^{i\omega_l t_2}) = \frac{|c_l| \sin(|c_l|^{-1} d_l(c_l e^{i\omega_l t_1}, c_l e^{i\omega_l t_2}))}{\sin\left(\frac{1}{2}(\pi - |c_l|^{-1} d_l(c_l e^{i\omega_l t_1}, c_l e^{i\omega_l t_2}))\right)} = 2|c_l| \sin\left(\tfrac{1}{2}(|c_l|^{-1} d_l(c_l e^{i\omega_l t_1}, c_l e^{i\omega_l t_2}))\right).$$

Thus, as a consequence of Theorem 2.9, $J_l \in \mathrm{bcd}_{r_l}^R(X_l, d_2)$ if and only if there exists a unique $[a, b) \in \mathrm{bcd}_{r_l}^R(X_l, d_l)$ such that

$$J_l = \left[2|c_l| \sin\left(\tfrac{1}{2}|c_l|^{-1} a\right), 2|c_l| \sin\left(\tfrac{1}{2}|c_l|^{-1} b\right)\right).$$

Furthermore, noting

$$d_l(c_l e^{i\omega_l t_1}, c_l e^{i\omega_l t_2}) = 2\pi |c_l| \bar{d}([\omega_l' t_1], [\omega_l' t_2]),$$

we can similarly say $[a, b) \in \mathrm{bcd}_{r_l}^R(X_l, d_l)$ if and only if there exists a unique $[a_0, b_0) \in \mathrm{bcd}_{r_l}^R(S_{\omega_l', T}, \bar{d})$ such that

$$[a, b) = [2\pi |c_l| a_0, 2\pi |c_l| b_0).$$

Combining these equivalences gives the desired result. □

4.1. ***Example.*** We execute the workflow illustrated in Figure 8, which takes as input a quasiperiodic function and produces the diagrams, for $T' \le T$,

$$\mathrm{dgm}_l^R(G_{T'}, d_\infty) \quad \text{for } l = 1, 2.$$

Concretely, we set

$$f(t) = \frac{1}{\sqrt{2}} e^{i\sqrt{3}t} + \frac{1}{\sqrt{2}} e^{i\sqrt{5}t}.$$

We then carry out three stages:

(1) Algorithm 1 (three-gap code): For each incommensurate frequency $\omega_j \in \{\sqrt{3}, \sqrt{5}\}$, run Algorithm 1 using the results from Section 3 to obtain the exact diagrams

$$\mathrm{dgm}_l^R(S_{\omega_j', T'}, \bar{d}) \quad \text{for } l = 1, 2 \text{ and } \omega_j' = \frac{\omega_j}{2\pi}.$$

(2) Persistent Künneth formula: Assemble these single-frequency outputs via Theorem 4.5 to obtain the diagrams

$$\mathrm{dgm}_l^R(G_{T'}, d_\infty) \quad \text{for } l = 1, 2.$$

(3) Error bounds: Finally, Theorem 4.3 provides an explicit bottleneck-distance bound showing that $\mathrm{dgm}_l^R(G_{T'}, d_\infty)$ approximates the true sliding-window diagram $\mathrm{dgm}_l^R(\mathrm{SW}_{d,\tau} f(T), d_2)$ within the claimed error.

Remark 4. In practical applications to real-world data, the frequencies ω_j are first estimated via the FFT of the observed time series (see Section 5).

With the roadmap in place, we begin by constructing the sliding-window embedding matrix as detailed at the end of Section 2.3. In our example one obtains

$$\mathrm{SW}_{d,\tau} f(t) = \frac{1}{\sqrt{d+1}} \begin{pmatrix} 1 & 1 \\ e^{i\sqrt{3}\tau} & e^{i\sqrt{5}\tau} \\ \vdots & \vdots \\ e^{i\sqrt{3}d\tau} & e^{i\sqrt{5}d\tau} \end{pmatrix} \begin{pmatrix} \tilde{c}_1 e^{i\sqrt{3}t} \\ \tilde{c}_2 e^{i\sqrt{5}t} \end{pmatrix},$$

where $\tilde{c}_1 = \tilde{c}_2 = \sqrt{d+1}/\sqrt{2}$.

We take

$$d = 1 \quad \text{and} \quad \tau = \frac{\pi}{\sqrt{3} - \sqrt{5}}.$$

With these parameters A is orthonormal. Hence

$$k = \max\{\sigma_{\min}^{-1}, \sigma_{\max}\sqrt{M}\} = \max\{1, \sqrt{2}\} = \sqrt{2}, \quad \text{where } M = 2.$$

Finally, we approximate the sliding-window point cloud

$$\mathbb{SW}_{d,\tau} f(2000)$$

using $T' = 500$. This sets the stage for fleshing out our 3G approximation method. We next apply Algorithm 1 to each frequency component in turn.

First, the scaled frequencies admit the continued-fraction expansions

$$\omega_1' = \frac{\sqrt{3}}{2\pi} = [0; 3, 1, 1, 1, 2, \dots] \quad \text{and} \quad \omega_2' = \frac{\sqrt{5}}{2\pi} = [0; 2, 1, 4, 3, 1, \dots].$$

By Corollaries 3.4 and 3.8, the resulting persistence diagrams are

$$\begin{aligned}
&\mathrm{dgm}_0^R(S_{\omega_1',500}, \bar{d}) = \{(0, 1.577 \times 10^{-3})^{160}, (0, 2.077 \times 10^{-3})^{316}, (0, 3.654 \times 10^{-3})^{24}, (0, \infty)\},\\
&\mathrm{dgm}_1^R(S_{\omega_1',500}, \bar{d}) = \{(3.654 \times 10^{-3}, 334.551 \times 10^{-3})\},\\
&\mathrm{dgm}_0^R(S_{\omega_2',500}, \bar{d}) = \{(0, 0.368 \times 10^{-3})^{161}, (0, 2.637 \times 10^{-3})^{220}, (0, 3.005 \times 10^{-3})^{119}, (0, \infty)\},\\
&\mathrm{dgm}_1^R(S_{\omega_2',500}, \bar{d}) = \{(3.005 \times 10^{-3}, 334.846 \times 10^{-3})\}.
\end{aligned}$$

With our single-frequency persistence diagrams in hand, we now apply the persistent Künneth formula (Theorem 4.5). Recall

$$G_{500} = \{(e^{i\omega_1 t_1}, e^{i\omega_2 t_2})\}_{0 \le t_1, t_2 \le 500}.$$

To verify the hypotheses of Theorem 4.3, we identify the diagrams of maximal persistence. From $\mathrm{dgm}_1^R(S_{\omega_1',500}, \bar{d})$ the interval $(a_1', b_1') = (3.654 \times 10^{-3}, 334.551 \times 10^{-3})$ induces in $\mathrm{dgm}_1^R(G_{500}, d_\infty)$ the interval

$$(a_1'', b_1'') = (2\sin(a_1'\pi), 2\sin(b_1'\pi)) = (0.02296, 1.73586).$$

Similarly, from $\mathrm{dgm}_1^R(S_{\omega_2',500}, \bar{d})$ with $(a_2', b_2') = (3.005 \times 10^{-3}, 334.846 \times 10^{-3})$ we obtain

$$(a_2'', b_2'') = (2\sin(a_2'\pi), 2\sin(b_2'\pi)) = (0.01888, 1.73678).$$

In $\mathrm{dgm}_2^R(G_{500}, d_\infty)$ the most persistent interval is $(a_3'', b_3'') = (0.02296, 1.73586)$.

Since $\lambda \le d_H(\phi_{2000}, G_{500}) = 0.20975$ and $\max\{k^2, 1\} = 2$, we compute

$$\frac{b_1'' - 2\lambda}{a_1'' + 2\lambda} = \frac{1.73586 - 2 \cdot 0.20975}{0.02296 + 2 \cdot 0.20975} = 2.9751 > 2 \quad \text{and} \quad \frac{b_2'' - 2\lambda}{a_2'' + 2\lambda} = \frac{1.73678 - 2 \cdot 0.20975}{0.01888 + 2 \cdot 0.20975} = 3.0049 > 2.$$

Thus the conditions of Theorem 4.3 are met. Define, for any x,

$$X(x) = \max\left\{0, \frac{x - 2\lambda}{k}\right\} \quad \text{and} \quad Y(x) = k(x + 2\lambda).$$

We compute the error bounds to be

$$\begin{aligned}
&(X(a_1''), Y(a_1'')) = (0, 0.6257), \quad (X(b_1''), Y(b_1'')) = (0.9308, 3.0481),\\
&(X(a_2''), Y(a_2'')) = (0, 0.6200), \quad (X(b_2''), Y(b_2'')) = (0.9315, 3.0494),\\
&(X(a_3''), Y(a_3'')) = (0, 0.6257), \quad (X(b_3''), Y(b_3'')) = (0.9308, 3.0481).
\end{aligned}$$

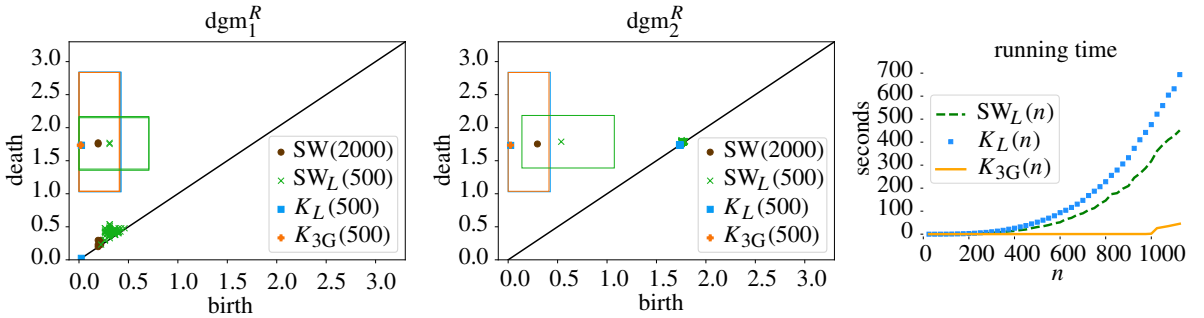

Figure 11. Persistence diagrams from Section 4.1. We also report the computation times for Ripser [Bauer 2016] on the sliding-window embedding (SW) and the method (K_L). Our implementation (K_{3G}) does not invoke Ripser at any stage.

Therefore Theorem 4.3 guarantees unique diagrams

$$(a_1, b_1), (a_2, b_2) \in \mathrm{dgm}_1^R(\mathbb{SW}_{d,\tau} f(2000), d_2) \quad \text{and} \quad (a_3, b_3) \in \mathrm{dgm}_2^R(\mathbb{SW}_{d,\tau} f(2000), d_2)$$

satisfying

$$\begin{aligned} 0 \le a_1 \le 0.6257, &\quad 0.9308 \le b_1 \le 3.0481, \\ 0 \le a_2 \le 0.6200, &\quad 0.9315 \le b_2 \le 3.0494, \\ 0 \le a_3 \le 0.6257, &\quad 0.9308 \le b_3 \le 3.0481. \end{aligned}$$

Finally, we compute the actual persistence diagrams of the sliding-window embedding for verification. By evaluating

$$\mathrm{dgm}_i^R(\mathbb{SW}_{d,\tau} f(2000), d_2) \quad \text{for } i = 1, 2,$$

one finds that the diagrams predicted by our 3G method are

$$(a_1, b_1) = (0.193, 1.771), \quad (a_2, b_2) = (0.194, 1.753) \quad \text{and} \quad (a_3, b_3) = (0.296, 1.753).$$

Each (a_i, b_i) lies within its respective error-bound rectangle, as shown in Figure 11. For comparison, we also include two alternative approximations — the sliding-window landmark method $\mathrm{SW}_L(n)$ and the landmark-based Künneth method $\mathrm{K}_L(n)$ [Gakhar and Perea 2019] — together with their corresponding error-bound rectangles and measured computation times for varying sample sizes n.

5. Applications

In this section, we will apply our pipeline, 3G, to the following examples: synthetic tremor signals in nonlinear tuned vibration absorbers as indicators of safe or unsafe operations [Detroux et al. 2015]; neuroscience, where quasiperiodicity is associated with task-specific functions in certain brain areas [Kaslik et al. 2022]; and celestial mechanics, where quasiperiodicity translates to favorable trajectories for missions [Gómez and Mondelo 2001]. We contribute to these fields by providing a faster alternative (see Figure 11 and Table 2) to analyze the reconstructed signals of potential quasiperiodic systems.

5.1. ***Methodology.*** We focus on dynamical systems whose flow Φ arises from a known system of ordinary differential equations. To generate a corresponding time series "observation", we solve these ODEs from a chosen initial condition and record the resulting solution values as the signal $f(t)$. We reconstruct the system by computing the sliding-window point cloud $\{\mathrm{SW}_{d,\tau} f(\epsilon t)\}_{t=0}^{T}$, where ϵ is chosen according to the Nyquist–Shannon sampling theorem [Shannon 1949]. The framework detailed in [Gakhar and Perea 2024] provides a method for selecting d and τ and approximating $\mathrm{dgm}_j^R(\{\mathrm{SW}_{d,\tau} f(\epsilon t)\}_{t=0}^{T}, d_2)$ with $\mathrm{dgm}_j^R(\{\mathrm{SW}_{d,\tau} S_1 f(\epsilon t)\}_{t=0}^{T}, d_2)$. Since $S_1 f$ is a sum of the form shown in Corollary 4.4, we can apply our result to approximate the latter, thus closely approximating the former. Indeed, in the examples we consider,

$$S_1 f(\epsilon t) = \sum_{j=1}^{2} c_j (e^{i\epsilon\omega_j t} + e^{-i\epsilon\omega_j t}).$$

Thus 3G can be used to approximate $\mathrm{dgm}_j^R(\{\mathrm{SW}_{d,\tau} S_1 f(\epsilon t)\}_{t=0}^{T}, d_2)$ with a known error bound as detailed in Remark 3.

5.2. ***Results.*** We consider systems with known quasiperiodic behavior, specifically those with two incommensurate frequencies. Hence the sliding-window point cloud $\{\mathrm{SW}_{d,\tau} f(\epsilon t)\}_{t=0}^{T}$ samples a 2-torus. We label the corresponding persistence diagrams as $\mathrm{SW}(T)$ (shown as brown dots). By $\mathrm{SW}_{S_1}(T)$, we denote the persistence diagrams of the sliding-window embedding $S_1(f)$ (shown as blue squares). The approximation obtained from 3G is labeled $K_{3G}(T)$ (shown as orange crosses).

5.2.1. *Double gyre.* The driven double gyre system provides a model for patterns occurring in geophysical flows [Shadden et al. 2005]. A topological approach to it has shown great success. Indeed, as shown in [Charó et al. 2020], there are multiple topological classifications that can be observed in the system representing the motion of a fluid particle. In this work, they noted that the motion of fluid can be sparse, meaning some initial conditions will imply a particle will be contained in a small region. Different initial conditions have shown trajectories with the topology of a standard strip, five-handle structure with torsion, torus, and möbius strip. This result was achieved by calculating homologies in a branched manifold while keeping track of the orientability chains, allowing for the identification of the branches and the localization of twists or torsions. This approach is called branched manifold analysis through homologies (BraMAH). At its core, it follows the principle of reconstructing a dynamical system from a time series. Yet the details at each step are completely different from SW. Nevertheless, for the corresponding initial conditions, we independently corroborated the presence of a torus, i.e., quasiperiodicity in the motion of the fluid particle; see Figure 12. This highlights the robustness offered by a topological approach to dynamical systems.

Concretely, the driven double gyre is given by the equation $\dot{x} = (-\partial\psi/\partial x_2, \partial\psi/\partial x_1)$, where

$$\psi(x_1, x_2, t) = A \sin(\pi g(x_1, t)) \sin(\pi x_2)$$

with

$$g(x_1, t) = \eta \sin(\lambda t)(x_1^2 - 2x_1) + x_1,$$

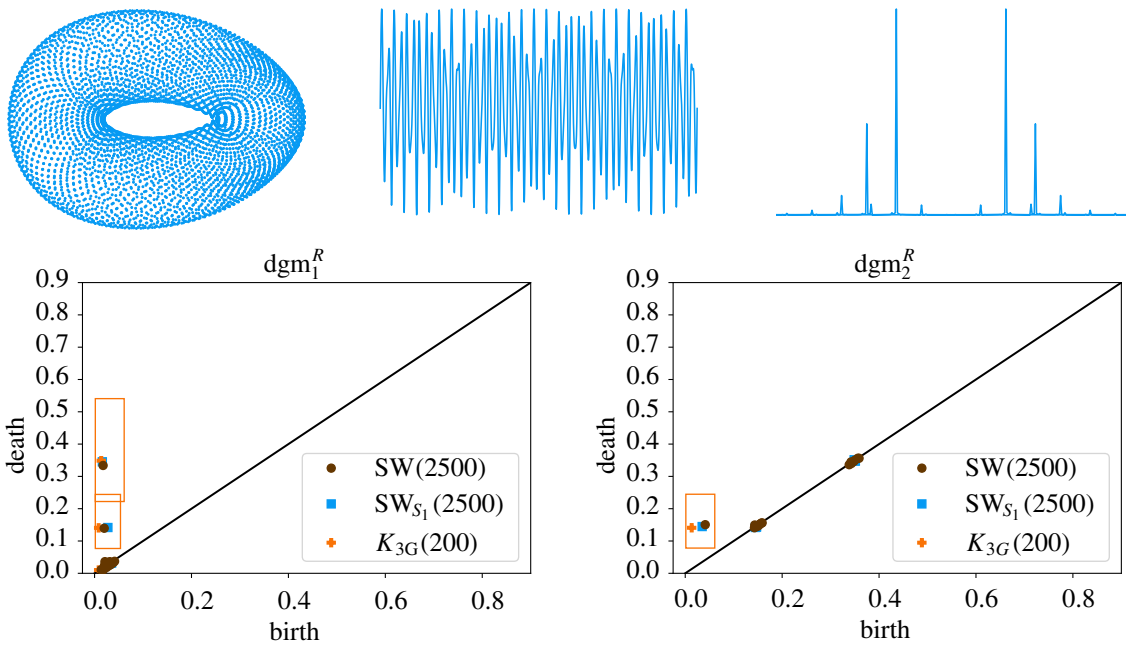

Figure 12. Top row: phase portrait of the driven double gyre system with initial condition x_0 (left), the corresponding trajectory $x_1(t)$ used for sliding-window embedding (center), and its Fourier power spectrum via FFT (right). Bottom row: the persistence diagrams of the resulting Rips filtrations for $x_1(t)$.

and parameter values A, $\mu = 0.1$ and $\lambda = \frac{1}{5}\pi$. The system has a toroidal attractor for the initial condition $x_0 = (0.5, 0.625)$ [Charó et al. 2020]. We solve the system using $dt = 0.1$ up to $t = 800$. Furthermore, SW is done using $f = x_1$, $d = 4$, $\tau = 119.03$ and $\epsilon = 0.1$.

5.2.2. *The torus.* We now consider a toroidal attractor in $\mathbb{R}^4$ with coordinates (x, y, z, r). The dynamical system is given by the set of equations

$$\dot{x} = -y + x(1 - \sqrt{x^2 + y^2}), \quad \dot{y} = x + y(1 - \sqrt{x^2 + y^2}),$$
$$\dot{z} = -kr + z(4 - \sqrt{z^2 + r^2}), \quad \dot{r} = kz + r(4 - \sqrt{z^2 + r^2}).$$

When k is irrational, the solutions span a torus [Penalva Vadell 2018]. We consider the case $k = \sqrt{2}$ with the initial condition $(x_0, y_0, z_0, r_0) = (1, 0, 4, 0)$. We solve the system with $dt = 0.1$ up to $t = 800$. The sliding window is done using $f = x + z$, $d = 4$, $\tau = 87.56$ and $\epsilon = 0.1$; see Figure 13.

5.2.3. *Pendulum attached to a sliding block.* We now consider a particular type of tuned mass damper (TMD). A TMD is a device used to suppress vibration by moving a mass attached to the main structure through springs and dampers [Wen et al. 2019]. This model has been successfully used to dampen the effect of long-duration earthquake ground motions [Murudi and Mane 2004]. Indeed, one can consider the main structure being a skyscraper and the incoming wave being generated by the earthquake. Thus a better understanding of this system translates to earthquake-resistant technologies.

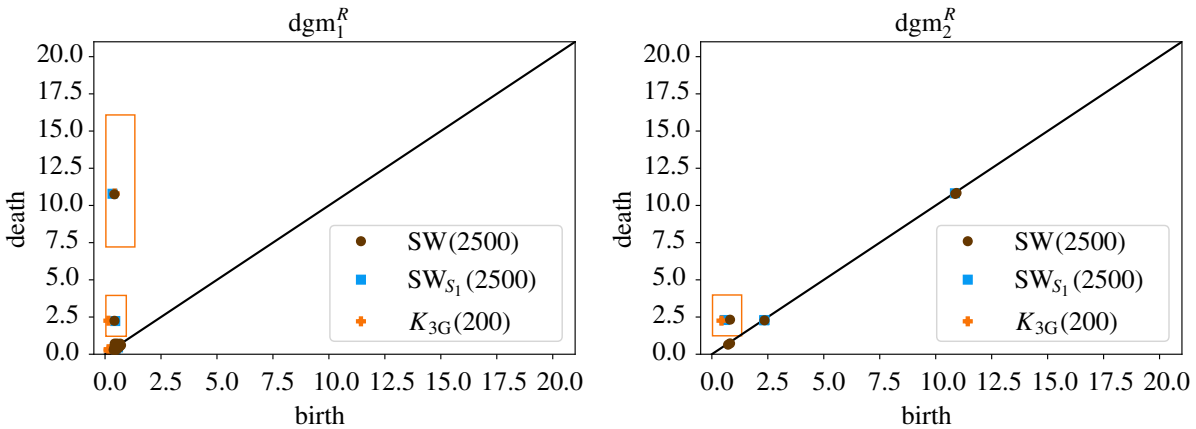

Figure 13. Diagrams obtained for the torus in $\mathbb{R}^4$.

We consider the case of a pendulum attached to a sliding block; see Figure 14. It was shown to exhibit quasiperiodicity in [Wen et al. 2019]. The governing equations are

$$\ddot{x} + \alpha^2 x - \bar{\epsilon} g\theta - \bar{\epsilon} L\dot{\theta}^2\theta = 0 \quad \text{and} \quad \ddot{\theta} + (1+\bar{\epsilon})\beta^2\theta - \bar{\epsilon} h\alpha^2 x + \bar{\epsilon}\dot{\theta}^2\theta = 0,$$

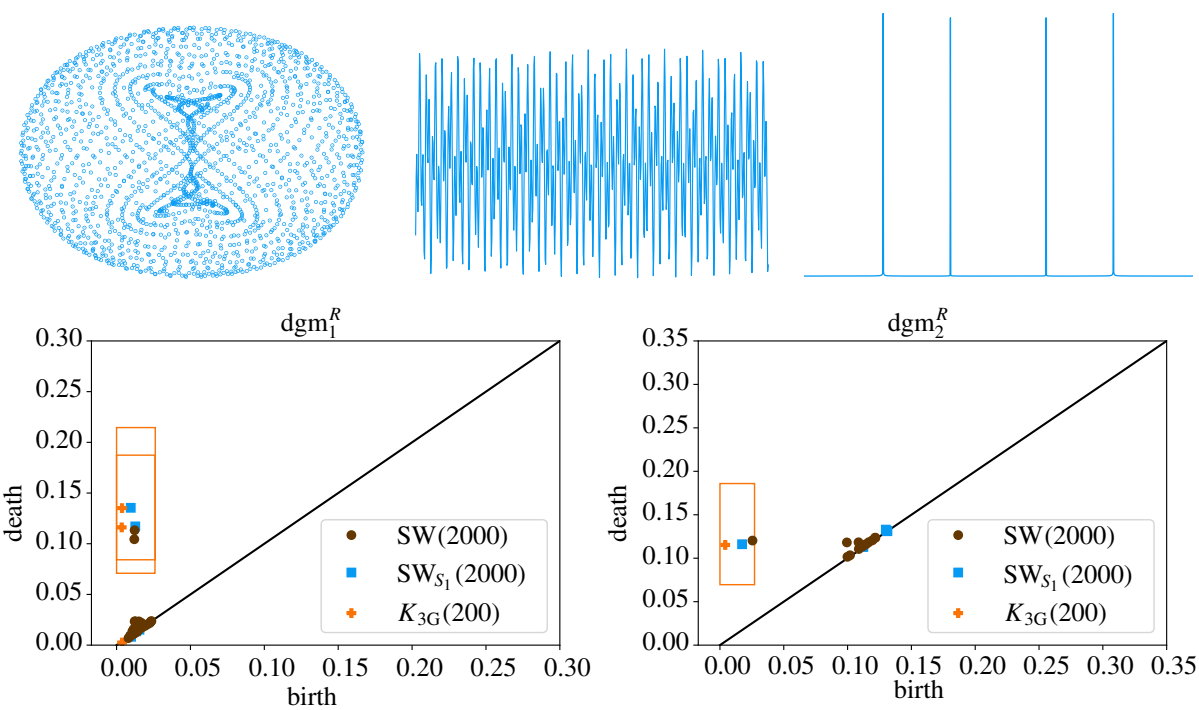

Figure 14. Top row: phase portrait $(x, \dot{x})$ of the pendulum on a sliding-block system (left), the scalar trajectory $x(t)$ used for sliding-window embedding (center), and its Fourier spectrum via FFT (right). Bottom row: persistence diagrams of the Rips filtration on the sliding-window point cloud derived from $x(t)$.

in which

$$\bar{\epsilon} = \frac{m}{M}, \quad \alpha = \sqrt{\frac{k}{M}}, \quad \beta = \sqrt{\frac{g}{L}}, \quad h = \frac{1}{\bar{\epsilon} L},$$

and g is the acceleration of gravity. The parameter values are $m = 0.5$, $M = 1$, $L = 1$ and $k = 5$. We solve the system with the initial condition $(x_0, \dot{x}_0, \theta_0, \dot{\theta}_0) = (0.1, 0, -0.1, 0)$ and $dt = 0.27$ up to $t = 540$. The sliding window is done using $f = x$, $d = 4$, $\tau = 108.05$ and $\epsilon = 0.027$.

5.2.4. *Generalized Wilson–Cowan equations.* We consider a generalized version of the Wilson–Cowan equations. Traditionally, these equations are derived via a time-coarse graining technique that averages the response. They also restrict to a weak gamma distribution of time delays. The extended model has been treated in [Kaslik et al. 2022], and is given by

$$\dot{u}(t) = -u(t) + f_1\left(\theta_u + \int_{-\infty}^{t} h(t-s)(au(s) + bv(s))\, ds\right),$$
$$\dot{v}(t) = -v(t) + f_2\left(\theta_v + \int_{-\infty}^{t} h(t-s)(cu(s) + dv(s))\, ds\right),$$

where $u(t)$ and $v(t)$ model the firing activity in two neuronal populations, a, b, c and d are the connection weights, and θ_u and θ_v are background drives. The activation functions f_1 and f_2 are smooth and increasing on the real line. We consider three types of delay kernels $h : [0, \infty) \to [0, \infty)$, namely, weak gamma, strong gamma and Dirac kernels. Their analysis indicates a preferable kernel based on the function of the model populations.

One can readily verify that this system recovers the Wilson–Cowan equations in the case of a weak gamma kernel. We consider the case of a Dirac kernel; see Figure 15. This system has been shown to exhibit quasiperiodicity [Kaslik et al. 2022; Coombes and Laing 2009]. Furthermore, it has applications to the subthalamic nucleus–globus pallidus network involved in Parkinson's disease (guided by anatomical and electrophysiological research) [Holgado et al. 2010]. The system of interest becomes

$$\dot{u}(t) = -u(t) + f_1(\theta_u + au(t-\tau_1) + bv(t-\tau_2)), \quad \dot{v}(t) = -v(t) + f_2(\theta_v + cu(t-\tau_2) + dv(t-\tau_1)),$$

where

$$f_1(x) = f_2(x) = \frac{1}{1 + e^{-\delta x}}.$$

The parameter values are $\theta_u = 0.1$, $\theta_v = 0.2$, $\tau_1 = \tau_2 = 0.152$, $a = d = -19$, $b = c = 10$ and $\delta = 10$. We solve the system with initial conditions $(u_0, v_0) = (0.05, 0.05)$ and $dt = 0.001$ up to $t = 50$. The sliding window is done using $f = u$, $d = 4$, $\tau = 1.712$ and $\epsilon = 0.01$.

5.2.5. *Electromagnetic radiation on a Wilson neuron model.* Wilson [1999] introduced a simplified model for a neocortical neuron by making assumptions on the Hodgkin–Huxley model. The biophysics of these neurons is governed by the interplay of about a dozen ion currents. His model showed the need for only four ion currents to accurately replicate known spiking behavior. We analyze an extension of his model that incorporates the presence of electromagnetic radiation (EMR).

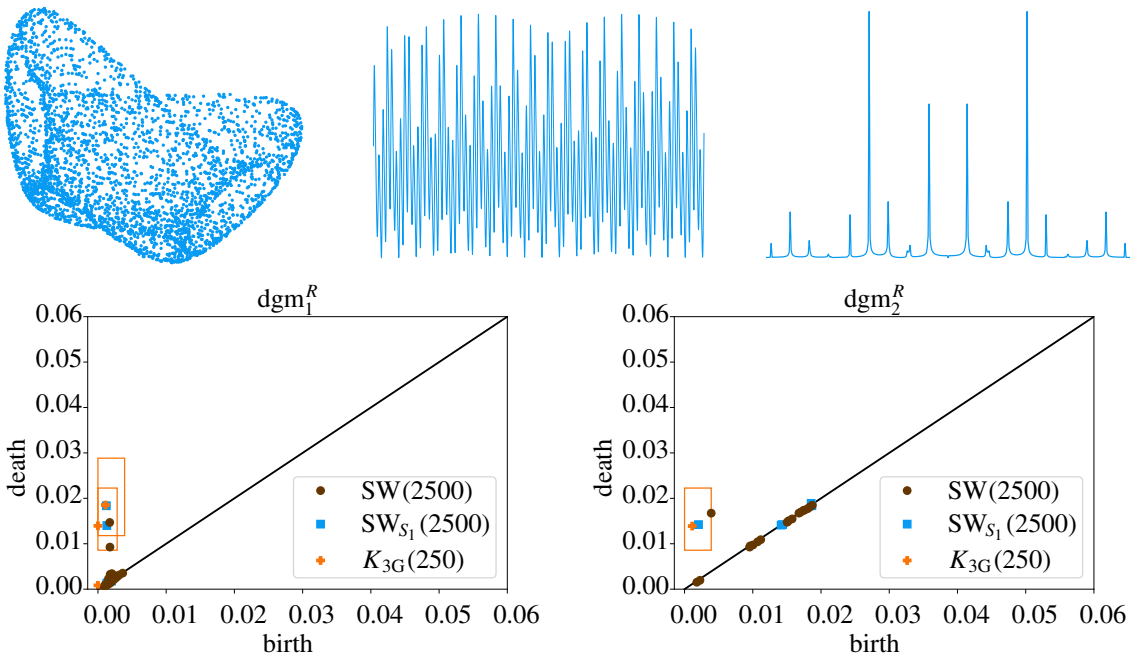

Figure 15. Top row: phase portrait (u, v) of the generalized Wilson–Cowan equations (left), the scalar trajectory $u(t)$ used for sliding-window embedding (center), and its Fourier power spectrum via FFT (right). Bottom row: persistence diagrams of the Rips filtration on the sliding-window point cloud derived from $u(t)$.

Commonplace presence of electronic devices introduces EMR exposure to neurons. The effects EMR has was imitated with the presence of a flux-controlled memristor in [Ju et al. 2022]. Their proposed model was shown to exhibit quasiperiodicity and their results were successfully replicated using a microcontroller unit-based hardware platform. Their mathematical model describes membrane potential v, recovery variable r and inner state of the memristor ϕ,

$$C_m \frac{dv}{dt} = -m_\infty(v)(v - E_{Na}) - g_K r(v - E_K) + I_{\text{ext}} - k_1 W(\phi) v,$$
$$\frac{dr}{dt} = \frac{1}{\tau_r}(-r + r_\infty(v)), \qquad \frac{d\phi}{dt} = v - k_2\phi + \phi_{\text{ext}},$$

where

$$m_\infty(v) = 17.8 + 47.6v + 33.8v^2 \quad \text{and} \quad r_\infty(v) = 1.24 + 3.7v + 3.2v^2.$$

We use typical model parameters for the membrane capacitor, $C_m = 1$, reverse potential for sodium and potassium, $E_{Na} = 0.5$ and $E_K = -0.95$, respectively, maximal conductance of potassium, $g_K = 26$, potassium ion channel activation time constant, $\tau_r = 5$, and external stimulus current $I_{\text{ext}} = 1$ [Xu et al. 2021]. The EMR external contribution is given by $\phi_{\text{ext}} = A \sin(2\pi F t)$, and the terms $k_1 W(\phi) v$ and $k_2\phi$ denote the induction current caused by variation of magnetic flux and the leakage of magnetic flux. The memductance of the memristor is given by $W(\phi) = a - b\tanh(\phi)$ [Bao et al. 2017]. The remaining

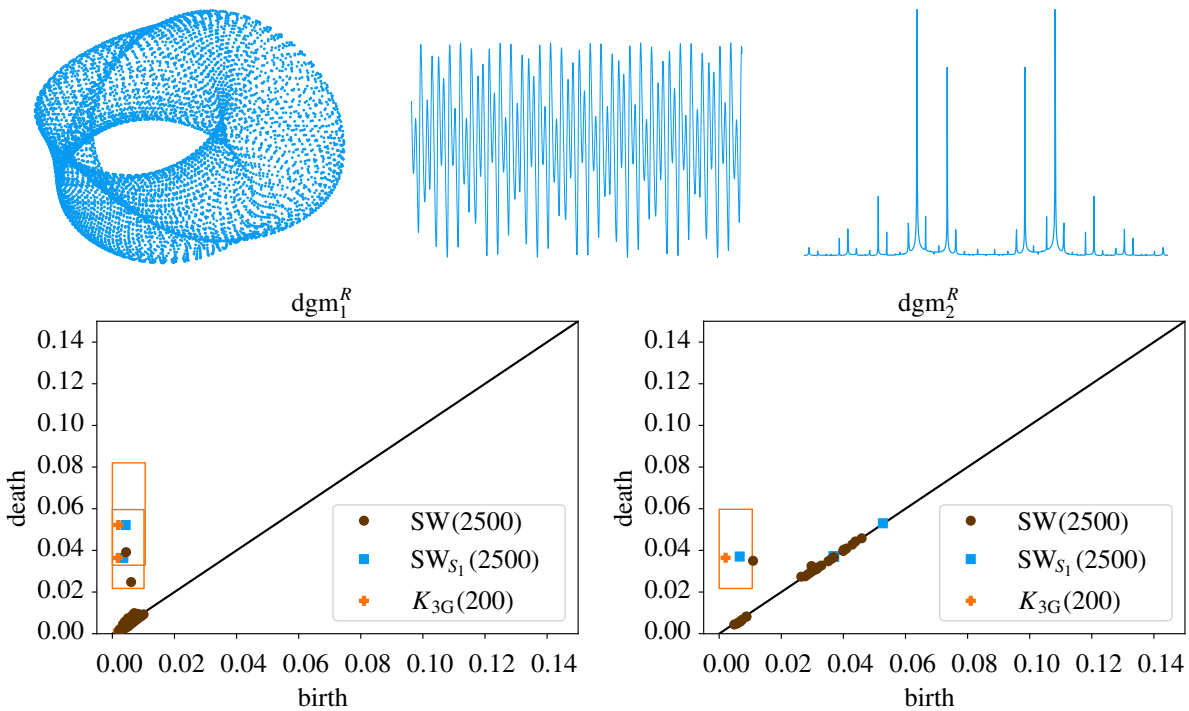

Figure 16. Top row: phase portrait (v, r, ϕ) of the system (left), the radial coordinate trajectory $r(t)$ used for sliding-window embedding (center), and its Fourier power spectrum via FFT (right). Bottom row: persistence diagrams of the Rips filtration on the sliding-window point cloud derived from $r(t)$.

parameter values are $a = 1$, $b = 3$, $k_1 = 1.2$, $k_2 = 0.5$, $A = 0.35$ and $F = 0.22$. We solve the system using the initial conditions $(v_0, r_0, \phi_0) = (0, 0, 0)$ and $dt = 0.01$ up to $t = 500$. The sliding window was done with $f = r$, $d = 4$, $\tau = 72.21$ and $\epsilon = 0.07$; see Figure 16.

5.2.6. *Competitive threshold-linear network.* Threshold-linear networks (TLNs) provide an accessible model incorporating a threshold nonlinearity [Morrison et al. 2024]. TLNs refine linear approximations of networks. The TLN model can be described by the equations

$$\frac{dx_i}{dt} = -x_i + \left[\sum_{j=1}^{n} W_{ij}x_j + b_i\right]_+$$

where $i = 1, \ldots, n$ and x_i represents the activity level of node i. The term W_{ij} is the directed connection strength, b_i is the external drive and $[y]_+ = \max\{y, 0\}$ is the threshold nonlinearity.

We consider competitive TLNs, where $W_{ij} \leq 0$, $W_{ii} = 0$ and $b_i \geq 1$. Furthermore, we consider the connection strength:

$$W_{ij} = \begin{cases} 0 & \text{if } i = j, \\ -1 + \lambda & \text{if node } j \text{ is connected to node } i, \\ -1 - \delta & \text{otherwise.} \end{cases}$$

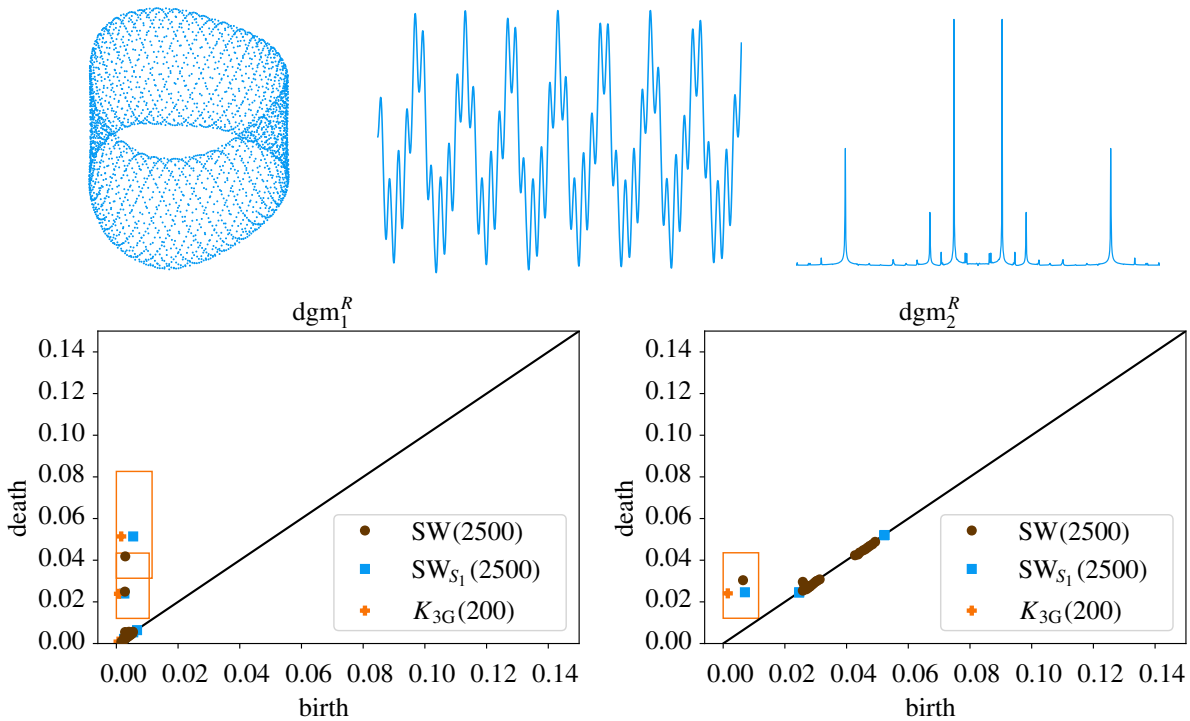

Figure 17. Top row: three-dimensional PCA projection of trajectories from the competitive TLN model (left), the scalar trajectory $x_4(t)$ used for sliding-window embedding (center), and its Fourier power spectrum via FFT (right). Bottom row: persistence diagrams of the Rips filtration on the sliding-window point cloud derived from $x_4(t)$.

This model has shown complex behavior, including quasiperiodicity. We replicate the quasiperiodic behavior of [Morrison et al. 2024, Figure 2] and refer to it for the initial condition and connection matrix. The remaining parameter values are $n = 25$, $b_i = 1$, $\lambda = 0.25$ and $\delta = 0.5$. We solve up to $t = 600$ and perform the sliding window with $f = x_4$, $d = 4$, $\tau = 27.53$ and $\epsilon = 0.07$; see Figure 17.

5.2.7. *Restricted three-body problem.* In celestial mechanics, the restricted three-body problem (RTBP) offers an accessible model with known equilibrium points [Koon et al. 2000]. The equations describe the progression of three celestial bodies in which one of them is considered a massless particle. The other two bodies, called primaries, are assumed to move in circular orbits around their center of mass. By taking a coordinate system that rotates with the primaries and under the appropriate scaling, it can be assumed the primaries have masses $1-\mu$ and μ, $\mu \in \left[0, \frac{1}{2}\right]$, are fixed at $(\mu, 0, 0)$ and $(\mu - 1, 0, 0)$, respectively, and complete one revolution in 2π [Gómez and Mondelo 2001]. This framework allows us to express the motion of the massless particle by the equations

$$\ddot{x} - 2\dot{y} = \Omega_x, \quad \ddot{y} + 2\dot{x} = \Omega_y, \quad \ddot{z} = \Omega_z,$$

where

$$\Omega = \tfrac{1}{2}(x^2 + y^2) + \frac{1-\mu}{r_1} + \frac{\mu}{r_2} + \tfrac{1}{2}\mu(1-\mu),$$

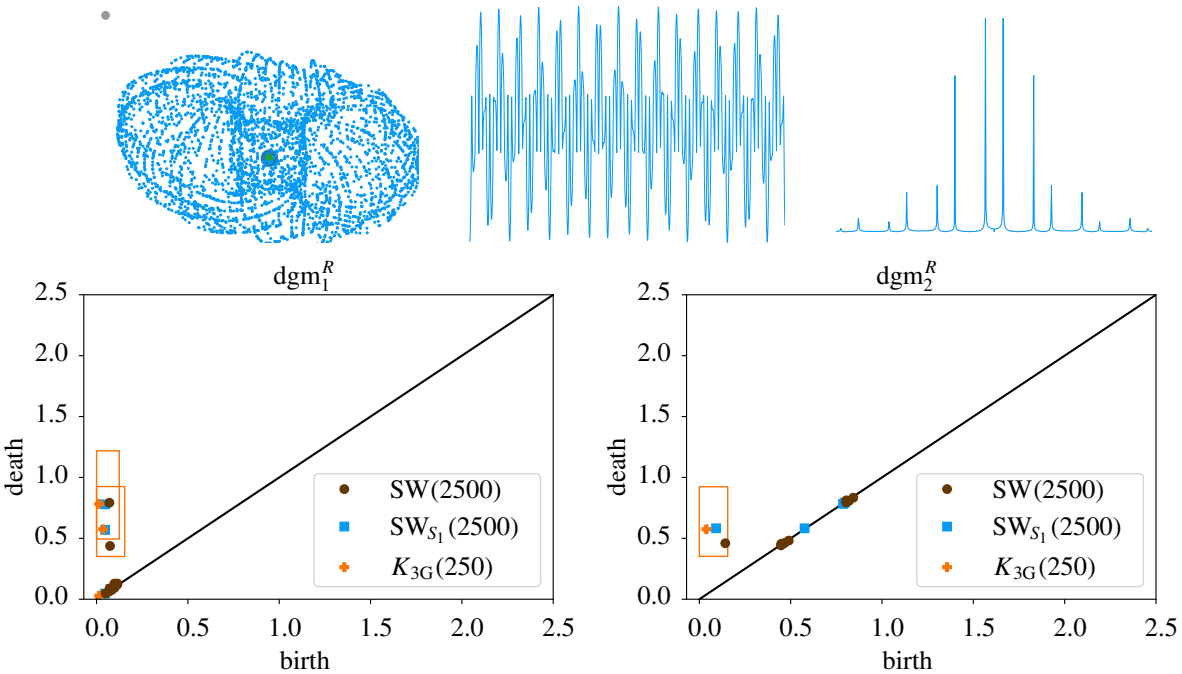

Figure 18. Top row: phase portrait of the restricted three-body problem in (x, y, z)-space, showing the Earth (blue/green) and the Moon (gray) as fixed primaries (left), the scalar trajectory $x(t)$ used for sliding-window embedding (center), and its Fourier power spectrum via FFT (right). Bottom row: persistence diagrams of the Rips filtrations on the sliding-window point cloud derived from $x(t)$.

and

$$r_1 = \sqrt{(x-\mu)^2 + y^2 + z^2} \quad \text{and} \quad r_2 = \sqrt{(x-\mu+1)^2 + y^2 + z^2}$$

are the distances from the particles to the primaries.

The case of the Earth–Moon system is of particular interest since it can aid in spacecraft missions interested in the Sun and the magnetosphere of the Earth [Gómez and Mondelo 2001]. Indeed, near the equilibrium points of the system, quasiperiodicity is present which translates to nice trajectories for a mission. We replicate this behavior for the Earth–Moon system; see Figure 18. In this case, $\mu = 0.0121506$. We solve the system with the initial condition $(x_0, y_0, z_0, \dot{x}, \dot{y}, \dot{z}) = (-0.5, 0, 0, 0, 0, 0.73)$ up to $t = 100$. The sliding window was done with $f = x$, $d = 4$, $\tau = 4.37$ and $\epsilon = 0.03$.

5.2.8. *Bicircular restricted four-body problem.* Considering the effects of the sun in the RTBP model gives rise to the bicircular restricted four-body problem (BCR4BP). The model is of importance for exploiting the force from the sun in trajectory designs for lunar missions and has found applications for ballistic lunar transfers to the lunar region [McCarthy and Howell 2023]. The new model uses the same coordinate axes as the RTBP and the same circular motion assumptions of the Earth and Moon, but it now includes terms pertaining to the influence of the Sun. The Sun is assumed to lie in the x–y plane at a fixed distance to the origin, a_4, and move with a constant angular velocity, $\dot{\theta}_S$, in circular motion.

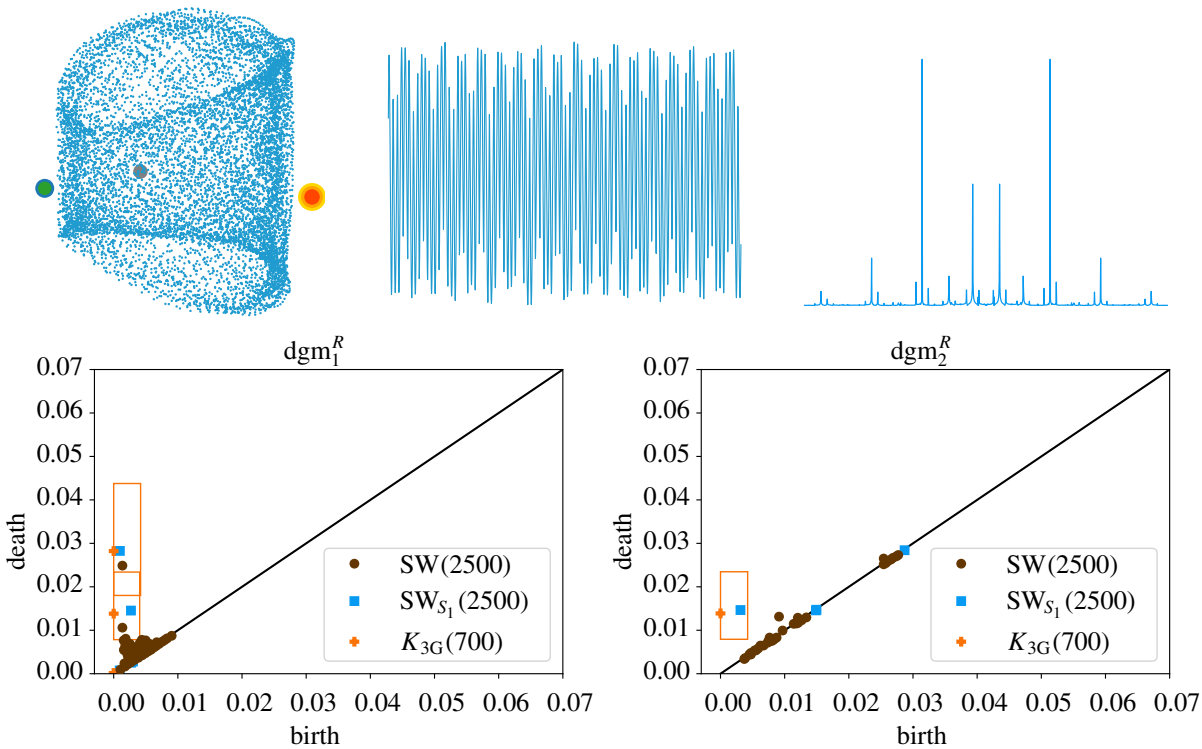

Figure 19. Top row: phase portrait of the bicircular restricted four-body problem in (x, y, z)-space, showing Earth (blue/green), Moon (gray), and Sun (red/yellow) as fixed primaries (positions not to scale). Center: the scalar trajectory $z(t)$ used for sliding-window embedding. Right: its Fourier power spectrum via FFT. Bottom row: persistence diagrams of the Rips filtrations on the sliding-window point cloud derived from $z(t)$.

Furthermore, the model assumes the Earth and Moon are not perturbed by solar gravity. Under these assumptions, the equations are [McCarthy and Howell 2023]

$$\ddot{x} = 2\dot{y} + \frac{\partial \Upsilon}{\partial x}, \quad \ddot{y} = -2\dot{x} + \frac{\partial \Upsilon}{\partial y}, \quad \ddot{z} = \frac{\partial \Upsilon}{\partial z},$$

where

$$\Upsilon = \frac{1-\mu}{r_{13}} + \frac{\mu}{r_{23}} + \tfrac{1}{2}(x^2 + y^2) + \lambda\left(\frac{m_4}{r_{43}} - \frac{m_4}{a_4^3}(x_4 x + y_4 y + z_4 z)\right),$$

and (x_4, y_4, z_4) denotes the position of the sun, r_{13}, r_{23} and r_{43} the distance of the Earth to the massless object, the Moon to the massless object, and the Sun to the massless object, respectively, and m_4 is the nondimensional mass of the Sun. We note that the case $\lambda = 0$ reduces to the RTBP. A study of the system as λ increases to 1 is done in [McCarthy and Howell 2023], where they showed the model exhibited quasiperiodicity. We replicate the quasiperiodic behavior (see Figure 19) for parameter values $\lambda = 1$, $\mu = 0.012155$, $a_4 = 388.84$, $m_4 = 328950.69$ and $\dot{\theta}_S = -0.9251986$. The system was solved with the initial condition $(x_0, y_0, z_0, \dot{x}, \dot{y}, \dot{z}, \theta_S) = (1.09, 0, 0, 0, 0.19, 0.05, 2)$ up to $t = 200$. The sliding window was done with $f = z$, $d = 4$, $\tau = 39.99$ and $\epsilon = 0.009$.

example	SW	SW(S1)	K_{3G}
5.2.1	7008.66	7672.85	0.87
5.2.2	4351.15	5351.15	0.42
5.2.3	3126.81	3218.73	0.50
5.2.4	5556.86	7628.48	0.98
5.2.5	5137.54	6505.54	0.66
5.2.6	5805.28	7193.97	0.22
5.2.7	6900.29	7937.03	2.09
5.2.8	6615.33	8231.25	0.59

Table 2. Running times, in seconds.

5.3. ***Concluding remarks.*** In this section, we detailed how our 3G method can be implemented on general quasiperiodic functions. Our approximation method was used on dynamical systems known to exhibit quasiperiodicity. As our figures show, we successfully approximated the diagrams obtained from SW. Error bounds can also be computed for our method, illustrated in the plots as rectangles. Furthermore, our approach significantly reduces computational time, as shown in Table 2. We hope our work contributes to the implementation of the sliding-window embedding technique on large data sets.

6. Conclusions and future work

We detailed how SW is a vital method used for better understanding of quasiperiodic signals. The correspondence between a quasiperiodic function of N incommensurate frequencies and an N-dimensional torus makes persistent homology an ideal component. However, the exponential computational cost of the latter limits the datasets that can be impacted by SW. Our contribution is providing an approximation to the persistence diagrams of interest (Section 4). Our method, 3G, achieves this within known error bounds. On average, our computation took less than 1 second to run for the examples depicted in Section 5. This contrasts with an average computation time of 5,563 seconds when using a standard library, Ripser [Bauer 2016], to compute the persistence diagrams of interest (Table 2).

Future work for our project would involve improving our approximation by tightening the error bounds. A more granular approach would be to inspect the specific transformation matrix instead of relying on a singular value argument. Another direction is to apply our work to real-world data, such as electrocardiogram datasets.

Appendix

Proposition A.1. *Let* $\sigma \in C_1(R_\epsilon(S_{\omega,T}))$ *and* $\sigma \neq 0$. *If* $\partial(\sigma) = 0$, *then there exist* $N \in \mathbb{N}$ *and* $\sigma_i \in C_1(R_\epsilon(S_{\omega,T}))$ *with* $\sigma_i \neq 0$, *such that*

$$\sigma = \sum_{i=0}^{N-1} \sigma_i,$$

$\partial(\sigma_i) = 0$ *and if* $\tau \subsetneq \sigma_i$,

$$\partial(\tau) \neq 0.$$

Moreover, σ_i *can be expressed as a sum of the form*

$$\sigma_i = \sum_{j=0}^{N_i - 1} [x_j, x_{j+1}],$$

where $x_i \in S_{\omega,T}$, $N_i \in \mathbb{N}$ *and* $x_{N_i} = x_0$.

Proof. Let $\tau_1 \subsetneq \sigma$ be such that $\partial(\tau_1) = 0$ and there are no $\bar{\tau} \subsetneq \sigma$ such that $\partial(\bar{\tau}) = 0$ and $\tau_1 \subsetneq \bar{\tau}$. If no such τ_1 exists, then let $\sigma_1 = \sigma$ and the result follows. Otherwise, let $\sigma_1 = \sigma/\tau_1$. By the maximality of τ_1, σ_1 satisfies the stated conditions. Now let $\tau_2 \subsetneq \tau_1$ be such that $\partial(\tau_2) = 0$ and there are no $\bar{\tau} \subsetneq \tau_1$ such that $\partial(\bar{\tau}) = 0$ and $\tau_2 \subsetneq \bar{\tau}$. If no such τ_2 exists, then let $\sigma_2 = \tau_1$ and the result follows. Otherwise, let $\sigma_2 = \tau_1/\tau_2$. As before, one can check σ_2 has the desired conditions. After finitely many steps, the process will stop resulting in the desired sum.

We now show σ_i can be expressed as stated. Note that since $\sigma_i \neq 0$, there exists $[x_0, x_1] \in \sigma_i$. Furthermore, since $\partial(\sigma_i) = 0$, there must exist a $[x_1, x_2] \in \sigma_i$ to cancel the term x_1. Similarly, there must also exist a term $[x_2, x_3] \in \sigma_i$ to cancel the term x_2. After repeating this process finitely many times, say N_i, we must reach a point with a term $[x_{N_i - 1}, x_0]$ to cancel the term x_0. Clearly

$$\partial\left(\sum_{j=0}^{N_i - 2} [x_j, x_{j+1}] + [x_{N_i - 1}, x_0] \right) = 0;$$

thus by the properties of σ_i, all of its terms must have been accounted for. □

For $[x, y] \in C_1(R_\epsilon(S_{\omega,T}))$, we let

$$L_{x,y} = 1$$

if in the circle representation of $S_{\omega,T}$, $\bar{d}(x, y)$ is the length of the arc starting at x and ending at y obtained by traversing clockwise. Similarly, we let

$$L_{x,y} = -1$$

if $\bar{d}(x, y)$ is the length of the arc traversing counterclockwise. Since $\bar{d}(x, y) \neq \frac{1}{2}$, for $x, y \in S_{\omega,T}$, $L_{x,y}$ is well defined. We now define

$$f([x, y]) = L_{x,y}\, \bar{d}(x, y).$$

Using linearity, we extend this function to all of $C_1(R_\epsilon(S_{\omega,T}))$, i.e., if $\sigma = \sum_i [x_i, y_i] \in C_1(R_\epsilon(S_{\omega,T}))$,

$$f(\sigma) = \sum_i f([x_i, y_i]) = \sum_i L_{x_i,y_i}\, \bar{d}(x_i, y_i).$$

Proposition A.2. *Let* $\sigma \in C_1(R_\epsilon(S_{\omega,T}))$, $f(\sigma) \neq 0$ *and* $N \in \mathbb{N}$ *such that*

$$\sigma = \sum_{i=0}^{N} [x_i, x_{i+1}].$$

If there exists an i_0 for which

$$L_{x_i,x_{i+1}} = \pm 1$$

for $0 \le i \le i_0$ and

$$L_{x_i,x_{i+1}} = \mp 1$$

for $i_0 < i \le N$, then σ is homologous to a

$$\bar{\sigma} = \sum_{i=0}^{\bar{N}} [\bar{x}_i, \bar{x}_{i+1}] \in C_1(R_\epsilon(S_{\omega,T})),$$

where $\bar{N} \in \mathbb{N}$, $\bar{x}_{i+1}$ is adjacent to $\bar{x}_i$ and

$$L_{\bar{x}_i,\bar{x}_{i+1}} = \operatorname{sgn}(f(\sigma)),$$

for $0 \le i \le \bar{N}$.

Proof. Without loss of generality we let

$$L_{x_i,x_{i+1}} = 1$$

for $0 \le i \le i_0$. Consider the circle representation of $S_{\omega,T}$. Let $\{x_j^0\}_{j=0}^{N_0}$ denote the points in the arc starting at x_0 and ending at x_1 traversing clockwise contained in $S_{\omega,T}$. We note $x_0^0 = x_0$ and $x_{N_0}^0 = x_1$. If $N_0 > 1$, one can verify

$$\sum_{j=0}^{N_0-1} [x_j^0, x_{j+1}^0] - [x_0, x_1] = \partial\left(\sum_{j=0}^{N_0-2} [x_j^0, x_{j+1}^0, x_{N_0}^0] \right),$$

i.e., $[x_0, x_1]$ is homologous to

$$\sigma_0 = \sum_{j=0}^{N_0-1} [x_j^0, x_{j+1}^0].$$

If $N_0 = 1$ we let $\sigma_0 = [x_0^0, x_{N_0}^0] = [x_0, x_1]$. By repeating this process, we construct σ_i for $0 \le i \le i_0$ such that

$$\sum_{i=0}^{i_0} \sigma_i = \sum_{i=0}^{i_0} \sum_{j=0}^{N_i-1} [x_j^i, x_{j+1}^i] = \sum_{i=0}^{A_1} [y_i, y_{i+1}],$$

where $y_0 = x_0$ and $y_{A_1+1} = x_{i_0+1}$, is homologous to

$$\sum_{i=0}^{i_0} [x_i, x_{i+1}].$$

Similarly, by considering the points in the arc starting at x_i and ending at x_{i+1}, for $i_0 < i \le N$, traversing counterclockwise contained in $S_{\omega,T}$, we can construct σ_i as before such that

$$\sum_{i=i_0+1}^{N} \sigma_i = \sum_{i=i_0+1}^{N} \sum_{j=0}^{N_i-1} [x_j^i, x_{j+1}^i] = \sum_{i=0}^{A_2} [\bar{y}_i, \bar{y}_{i+1}],$$

where $\bar{y}_0 = x_{i_0+1}$ and $\bar{y}_{A_2+1} = x_{N+1}$, is homologous to

$$\sum_{i=i_0+1}^{N} [x_i, x_{i+1}].$$

We note $y_{A_1+1} = \bar{y}_0 = x_{i_0+1}$ and $y_{A_1} = \bar{y}_1$ since the points of the clockwise arc, σ_{i_0}, end where the points of the counterclockwise arc, σ_{i_0+1}, start. Thus $[y_{A_1}, y_{A_1-1}] = -[\bar{y}_0, \bar{y}_1]$ and

$$\sum_{i=0}^{N} \sigma_i = \sum_{i=0}^{A_1-1} [y_i, y_{i+1}] + \sum_{i=1}^{A_2} [\bar{y}_i, \bar{y}_{i+1}].$$

Repeating this argument $A = \min\{A_1 + 1, A_2 + 1\}$ times, we conclude $[y_{A_1-i}, y_{A_1-i+1}] = -[\bar{y}_i, \bar{y}_{i+1}]$ for $0 \leq i < A$. We note that by construction

$$f\left(\sum_{i=0}^{A_1} [y_i, y_{i+1}] + \sum_{i=0}^{A_2} [\bar{y}_i, \bar{y}_{i+1}] \right) = f(\sigma) \neq 0.$$

Thus $A_1 \neq A_2$; i.e.,

$$\sum_{i=0}^{N} \sigma_i = \sum_{i=0}^{A_1-A_2-1} [y_i, y_{i+1}] \quad \text{or} \quad \sum_{i=0}^{N} \sigma_i = \sum_{i=A_1+1}^{A_2} [\bar{y}_i, \bar{y}_{i+1}]. \qquad \square$$

Corollary A.3. *Let $\sigma \in C_1(R_\epsilon(S_{\omega,T}))$ and $\partial(\sigma) = 0$. Then σ is homologous to 0 if and only if $f(\sigma) = 0$.*

Proof. By Proposition A.1, σ can be expressed as

$$\sum_{i=0}^{N-1} [x_i, x_{i+1}],$$

where $x_i \in S_{\omega,T}$, $N \in \mathbb{N}$ and $x_N = x_0$. The result follows by noting that in Proposition A.2, $f(\sigma) = 0$ if and only if $A_1 = A_2$, which happens if and only if σ is homologous to 0. $\square$

For the following result we let $\{x_i\}_{i=0}^{T}$ denote the elements of $S_{\omega,T}$ in ascending order, $\oplus$ denote mod $T + 1$ addition, and $k \in \mathbb{N}$.

Lemma A.4. *Let $\sigma \in C_1(R_\epsilon(S_{\omega,T}))$ be such that $\partial(\sigma) = 0$ and σ is not homologous to 0. Then σ is homologous to*

$$k \sum_{i=0}^{T} [x_i, x_{i\oplus 1}].$$

Proof. By Proposition A.1, we can express σ as

$$\sum_{i=0}^{N-1} [\bar{x}_i, \bar{x}_{i+1}],$$

where $\bar{x}_i \in S_{\omega,T}$, $N \in \mathbb{N}$, and $\bar{x}_N = \bar{x}_0$. Furthermore, by repeated application of Proposition A.2, σ is homologous to

$$\bar{\sigma} = \sum_{i=0}^{N_0} [y_i, y_{i+1}],$$

where $y_i \in S_{\omega,T}$, $N_0 \in \mathbb{N}$, $y_{N_0+1} = y_0$, y_{i+1} is adjacent to y_i and

$$L_{y_i, y_{i+1}} = \operatorname{sgn}(f(\sigma))$$

for $0 \le i \le N_0$. We note that a necessary condition to cancel a term $[y_i, y_{i+1}]$ is the existence of term $[y_{n_i}, y_{n_i+1}]$ for which

$$L_{y_{n_i}, y_{n_i+1}} = -\operatorname{sgn}(f(\sigma)).$$

Since this can't happen, we conclude the expression for $\bar{\sigma}$ can't be reduced. Furthermore, we note that by construction $T \le N_0$. Indeed, the minimal number j_0 of terms needed to obtain

$$\partial\left(\sum_{i=0}^{j_0} [y_i, y_{i+1}]\right) = 0$$

is $j_0 = T$ since this covers all of the points in $S_{\omega,T}$. We conclude

$$\sum_{i=0}^{T} [y_i, y_{i+1}] = \sum_{i=0}^{T} [x_i, x_{i\oplus 1}].$$

In fact, an application of Proposition A.1 to $\bar{\sigma}$ shows

$$\bar{\sigma} = \sum_{i=0}^{N_2-1} \sigma_i$$

for some $N_2 \in \mathbb{N}$. By the properties of σ_i and what has been shown, we conclude

$$\sigma_i = \sum_{j=0}^{T} [x_j, x_{j\oplus 1}]$$

for all $0 \le i \le N_2 - 1$. □

Lemma A.5. *Let $T \in \mathbb{N}$ and $\omega \in \mathbb{R}\backslash\mathbb{Q}$ with continued-fraction expansion $[a_1, a_2, a_3, \dots]$ and i-th convergent p_i/q_i, and k, r and s be the unique numbers for which*

$$q_k + q_{k-1} \le T < q_k + q_{k+1}$$

and

$$T = rq_k + q_{k-1} + s \quad \text{for } 1 \le r \le a_{k+1} \text{ and } 0 \le s \le q_k - 1.$$

Let

$$D_i = q_i\omega - p_i.$$

We assume

$$s+1 < q_k \quad \textit{and} \quad |D_{k+1}| + (a_{k+1} - r + 1)|D_k| < \tfrac{1}{3}.$$

Let Γ *be the set containing the pairs* (x, y) *for* $x, y \in S_{\omega,T}$ *and* $x < y$, *for which there exists a* $z \in ([0, x) \cup (y, 1)) \cap S_{\omega,T}$ *such that* $1 - \bar{d}(x, y) \leq 2\max\{\bar{d}(y, z), \bar{d}(x, z)\} \leq 2\,\bar{d}(x, y)$. *If*

$$\lambda = \min\{\bar{d}(x, y) \mid (x, y) \in \Gamma\},$$

then for $\epsilon \in (|D_{k+1}| + (a_{k+1} - r + 1)|D_k|, \lambda)$,

$$[\sigma] = 0$$

in $H_1(R_\epsilon(S_{\omega,T}, \bar{d}); \mathbb{F})$.

Proof. Let us write $\delta_C = |D_{k+1}| + (a_{k+1} - r + 1)|D_k|$. Since $\delta_C < \frac{1}{3}$ and ω is irrational, $\lambda > \delta_C$; thus ϵ is well defined. To show the result, it is sufficient to show there does not exists a $\tau \in C_2(R_\epsilon(S_{\omega,T}))$ such that

$$\sigma = \partial(\tau).$$

We will assume such τ exists and arrive at a contradiction. Thus suppose there exists a $\tau \in C_2(R_\epsilon(S_{\omega,T}))$ such that

$$\sigma = \partial(\tau).$$

Let

$$\lambda_0 = \max\{\bar{d}(x, y), \bar{d}(y, z), \bar{d}(z, y)\} \mid \text{there exists } [x, y, z] \in \tau\}.$$

Let $y_1, y_2 \in S_{\omega,T}$ for $y_1 < y_2$ be such that $\bar{d}(y_1, y_2) = \lambda_0$. By assumption there exists $y_3 \in S_{\omega,T}$ such that $[y_1, y_2, y_3] \in \tau$ or $[y_1, y_3, y_2] \in \tau$. We note that by construction

$$\max\{\bar{d}(y_2, y_3), \bar{d}(y_1, y_3)\} \leq \bar{d}(y_1, y_2).$$

Furthermore, without loss of generality we can assume $y_3 \in ([0, y_1) \cup (y_2, 1))$. Indeed, let us suppose $y_3 \in (y_1, y_2)$. There must exist a term of the form $[y_1, y_2, z_0]$ to cancel the term $-[y_1, y_2]$ in the case of the term $[y_1, y_3, y_2]$. In the case of the term $[y_1, y_2, y_3]$ take $z_0 = y_3$. If $z_0 \in ([0, y_1) \cup (y_2, 1))$ we are done. Thus we assume $z_0 \in (y_1, y_2)$. This implies there must exists a term $[y_1, z_0, z_1] \in \tau$ to cancel the term $-[y_1, z_0]$ from $\partial([y_1, y_2, z_0])$. If $z_1 \in (y_1, y_2)$, there must be a term of the form $[y_1, z_1, z_2] \in \tau$ to cancel the term $-[y_1, z_1]$ from $\partial([y_1, z_0, z_1])$. On the other hand, if $z_1 \in ([0, y_1) \cup (y_2, 1))$ we note

$$L_{y_1,z_1} = -L_{y_1,y_2},$$

or otherwise

$$\bar{d}(y_1, z_1) > \bar{d}(y_1, y_2),$$

a contradiction. As before, there must exists a $[z_0, z_2, z_1]$ to cancel the term $[z_0, z_1]$ from $\partial([y_1, z_0, z_1])$. Since in both scenarios we end up in a case analogous to the term $[y_1, y_2, z_0]$, we conclude this process won't end. Thus without loss of generality we assume $y_3 \in ([0, y_1) \cup (y_2, 1))$, as stated. We note

$$L_{y_1,y_2} = L_{y_2,y_3}$$

since otherwise $\bar{d}(y_2, y_3) > \bar{d}(y_1, y_2) = \lambda_0$, a contradiction. Similarly, it must be the case that

$$L_{y_1,y_2} = L_{y_3,y_1}$$

since otherwise $\bar{d}(y_3, y_1) > \bar{d}(y_1, y_2) = \lambda_0$. These two conditions imply

$$1 - \bar{d}(y_1, y_2) = \bar{d}(y_2, y_3) + \bar{d}(y_3, y_1) \leq 2 \max\{\bar{d}(y_2, y_3), \bar{d}(y_1, y_3)\},$$

i.e., $(y_1, y_2) \in \Gamma$, but since

$$\lambda_0 \leq \epsilon < \lambda$$

this is impossible by the minimality of λ. Thus no such τ exists. □

Acknowledgements

The authors would like to thank Facundo Mémoli and the referees for their detailed comments; they were invaluable in fixing multiple imprecisions found in the original draft.

References

[Bao et al. 2017] B. Bao, H. Qian, Q. Xu, M. Chen, J. Wang, and Y. Yu, "Coexisting behaviors of asymmetric attractors in hyperbolic-type memristor based Hopfield neural network", *Front. Comput. Neurosci.* **11** (2017), art. id. 81.

[Bauer 2016] U. Bauer, "Ripser", GitHub repository, 2016, available at https://github.com/Ripser/ripser.

[Bauer 2021] U. Bauer, "Ripser: efficient computation of Vietoris–Rips persistence barcodes", *J. Appl. Comput. Topol.* **5**:3 (2021), 391–423. MR

[Belloy et al. 2017] M. Belloy, M. Naeyaert, G. Keliris, A. Abbas, S. Keilholz, A. Van Der Linden, and M. Verhoye, "Dynamic resting state fmri in mice: detection of quasi-periodic patterns", conference presentation 0961, ISMRM, 2017, available at https://cds.ismrm.org/protected/17MProceedings/PDFfiles/0961.html.

[Beresnevich and Leong 2017] V. Beresnevich and N. Leong, "Sums of reciprocals and the three distance theorem", preprint, 2017. arXiv 1712.03758

[Charó et al. 2020] G. D. Charó, G. Artana, and D. Sciamarella, "Topology of dynamical reconstructions from Lagrangian data", *Phys. D* **405** (2020), art. id. 132371. MR

[Chazal et al. 2016] F. Chazal, V. de Silva, M. Glisse, and S. Oudot, *The structure and stability of persistence modules*, Springer, 2016. MR

[Cohen-Steiner et al. 2007] D. Cohen-Steiner, H. Edelsbrunner, and J. Harer, "Stability of persistence diagrams", *Discrete Comput. Geom.* **37**:1 (2007), 103–120. MR

[Coombes and Laing 2009] S. Coombes and C. Laing, "Delays in activity-based neural networks", *Philos. Trans. R. Soc. Lond. Ser. A Math. Phys. Eng. Sci.* **367**:1891 (2009), 1117–1129. MR

[Crawley-Boevey 2015] W. Crawley-Boevey, "Decomposition of pointwise finite-dimensional persistence modules", *J. Algebra Appl.* **14**:5 (2015), art. id. 1550066. MR

[Detroux et al. 2015] T. Detroux, G. Habib, L. Masset, and G. Kerschen, "Performance, robustness and sensitivity analysis of the nonlinear tuned vibration absorber", *Mech. Syst. Signal Process.* **60–61** (2015), 799–809.

[Gakhar and Perea 2019] H. Gakhar and J. A. Perea, "Künneth formulae in persistent homology", preprint, 2019. arXiv 1910.05656

[Gakhar and Perea 2024] H. Gakhar and J. A. Perea, "Sliding window persistence of quasiperiodic functions", *J. Appl. Comput. Topol.* **8**:1 (2024), 55–92. MR

[Gómez and Mondelo 2001] G. Gómez and J. M. Mondelo, "The dynamics around the collinear equilibrium points of the RTBP", *Phys. D* **157**:4 (2001), 283–321. MR

[Hatcher 2002] A. Hatcher, *Algebraic topology*, Cambridge Univ. Press, 2002. MR

[Hlawka et al. 1991] E. Hlawka, J. Schoissengeier, and R. Taschner, *Geometric and analytic number theory*, Springer, 1991. MR

[Holgado et al. 2010] A. J. N. Holgado, J. R. Terry, and R. Bogacz, "Conditions for the generation of beta oscillations in the subthalamic nucleus–globus pallidus network", *J. Neurosci.* **30**:37 (2010), 12340–12352.

[Ju et al. 2022] Z. Ju, Y. Lin, B. Chen, H. Wu, M. Chen, and Q. Xu, "Electromagnetic radiation induced non-chaotic behaviors in a Wilson neuron model", *Chinese J. Phys.* **77** (2022), 214–222. MR

[Kaslik et al. 2022] E. Kaslik, E.-A. Kokovics, and A. Rădulescu, "Stability and bifurcations in Wilson–Cowan systems with distributed delays, and an application to basal ganglia interactions", *Commun. Nonlinear Sci. Numer. Simul.* **104** (2022), art. id. 105984. MR

[Khasawneh and Munch 2016] F. A. Khasawneh and E. Munch, "Chatter detection in turning using persistent homology", *Mech. Syst. Signal Process.* **70–71** (2016), 527–541.

[Kim and Jung 2026] K. Kim and J.-H. Jung, "Exact multi-parameter persistent homology of time-series data: fast and variable topological inferences", *Adv. in Appl. Math.* **174** (2026), art. id. 103023. MR

[Koon et al. 2000] W. S. Koon, M. W. Lo, J. E. Marsden, and S. D. Ross, "Heteroclinic connections between periodic orbits and resonance transitions in celestial mechanics", *Chaos* **10**:2 (2000), 427–469. MR

[Leong 2017] N. Leong, *Sums of reciprocals and the three distance theorem*, Ph.D. thesis, University of York, 2017, available at https://etheses.whiterose.ac.uk/id/eprint/17431/.

[Lesnick 2015] M. Lesnick, "The theory of the interleaving distance on multidimensional persistence modules", *Found. Comput. Math.* **15**:3 (2015), 613–650. MR

[Levine and Steinhardt 1984] D. Levine and P. J. Steinhardt, "Quasicrystals: a new class of ordered structures", *Phys. Rev. Lett.* **53** (Dec 1984), 2477–2480.

[McCarthy and Howell 2023] B. P. McCarthy and K. C. Howell, "Four-body cislunar quasi-periodic orbits and their application to ballistic lunar transfer design", *Adv. Space Res.* **71**:1 (2023), 556–584.

[Morozov 2005] D. Morozov, "Persistence algorithm takes cubic time in the worst case", BioGeometry News, Department of Computer Science, Duke University, 2005, available at https://www.mrzv.org/publications/worst-case/biogeometry/.

[Morrison et al. 2024] K. Morrison, A. Degeratu, V. Itskov, and C. Curto, "Diversity of emergent dynamics in competitive threshold-linear networks", *SIAM J. Appl. Dyn. Syst.* **23**:1 (2024), 855–884. MR

[Murudi and Mane 2004] M. M. Murudi and S. M. Mane, "Seismic effectiveness of tuned mass damper (tmd) for different ground motion parameters", art. id. 2325 in 13*th World Conference on Earthquake Engineering* (Vancouver, BC, 2004), 2004.

[Myers and Khasawneh 2022] A. D. Myers and F. A. Khasawneh, "Damping parameter estimation using topological signal processing", *Mech. Syst. Signal Process.* **174** (2022), art. id. 109042.

[Olds 1963] C. D. Olds, *Continued fractions*, Random House, New York, 1963. MR

[Penalva Vadell 2018] J. Penalva Vadell, *Takens' theorem: proof and applications*, master's thesis, Universitat de les Illes Balears, 2018, available at http://hdl.handle.net/11201/149295.

[Perea 2019] J. A. Perea, "Topological times series analysis", *Notices Amer. Math. Soc.* **66**:5 (2019), 686–694. MR

[Perea et al. 2015] J. A. Perea, A. Deckard, S. B. Haase, and J. Harer, "SW1PerS: sliding windows and 1-persistence scoring; discovering periodicity in gene expression time series data", *BMC Bioinformatics* **16** (2015), art. id. 257.

[van Ravenstein 1988] T. van Ravenstein, "The three gap theorem (Steinhaus conjecture)", *J. Austral. Math. Soc. Ser. A* **45**:3 (1988), 360–370. MR

[Rockett and Szüsz 1992] A. M. Rockett and P. Szüsz, *Continued fractions*, World Sci., River Edge, NJ, 1992. MR

[Shadden et al. 2005] S. C. Shadden, F. Lekien, and J. E. Marsden, "Definition and properties of Lagrangian coherent structures from finite-time Lyapunov exponents in two-dimensional aperiodic flows", *Phys. D* **212**:3-4 (2005), 271–304. MR

[Shannon 1949] C. E. Shannon, "Communication in the presence of noise", *Proc. I.R.E.* **37** (1949), 10–21. MR

[Skraba et al. 2012] P. Skraba, V. De Silva, and M. Vejdemo-Johansson, "Topological analysis of recurrent systems", pp. 1–5 in *NIPS Workshop on Algebraic Topology and Machine Learning* (Lake Tahoe, NV, 2012), 2012.

[Takens 1981] F. Takens, "Detecting strange attractors in turbulence", pp. 366–381 in *Dynamical systems and turbulence* (Coventry, 1979/1980), Lecture Notes in Math. **898**, Springer, 1981. MR

[Tralie and Perea 2018] C. J. Tralie and J. A. Perea, "(Quasi)periodicity quantification in video data, using topology", *SIAM J. Imaging Sci.* **11**:2 (2018), 1049–1077. MR

[Weixing et al. 1993] D. Weixing, H. Wei, W. Xiaodong, and C. X. Yu, "Quasiperiodic transition to chaos in a plasma", *Phys. Rev. Lett.* **70** (1993), 170–173.

[Wen et al. 2019] R. Wen, T. Li, and B. Zhen, "Quasi-periodic motions of a pendulum with vibrating suspension point", *J. Vib. Eng. Technol.* **7** (2019), 519–532.

[Wilden et al. 1998] I. Wilden, H. Herzel, G. Peters, and G. Tembrock, "Subharmonics, biphonation, and deterministic chaos in mammal vocalization", *Bioacoustics* **9**:3 (1998), 171–196.

[Wilson 1999] H. R. Wilson, "Simplified dynamics of human and mammalian neocortical neurons", *J. Theoret. Biol.* **200**:4 (1999), 375–388.

[Xu et al. 2019] B. Xu, C. J. Tralie, A. Antia, M. Lin, and J. A. Perea, "Twisty Takens: a geometric characterization of good observations on dense trajectories", *J. Appl. Comput. Topol.* **3**:4 (2019), 285–313. MR

[Xu et al. 2021] Q. Xu, Z. Ju, C. Feng, H. Wu, and M. Chen, "Analogy circuit synthesis and dynamics confirmation of a bipolar pulse current-forced 2D Wilson neuron model", *Eur. Phys. J. Spec. Topics* **230**:7 (2021), 1989–1997.

[Yirka 2013] B. Yirka, "Japanese companies develop quake damping pendulums for tall buildings", online article, 2013, available at https://phys.org/news/2013-08-japanese-companies-quake-damping-pendulums.html.

[Zhigljavsky and Aliev 1999] A. Zhigljavsky and I. Aliev, "Weyl sequences: asymptotic distributions of the partition lengths", *Acta Arith.* **88**:4 (1999), 351–361. MR

[Zomorodian and Carlsson 2005] A. Zomorodian and G. Carlsson, "Computing persistent homology", *Discrete Comput. Geom.* **33**:2 (2005), 249–274. MR

Received 31 Oct 2023. Revised 16 Dec 2025.

LUIS SUAREZ SALAS:

suarezs3@msu.edu
Michigan State University, East Lansing, MI, United States

JOSE A. PEREA:

j.pereabenitez@northeastern.edu
Northeastern University, Boston, MA, United States